



HAL
open science

Hybrid-dimensional modelling of two-phase flow through fractured porous media with enhanced matrix fracture transmission conditions

K Brenner, J Hennicker, R Masson, P Samier

► **To cite this version:**

K Brenner, J Hennicker, R Masson, P Samier. Hybrid-dimensional modelling of two-phase flow through fractured porous media with enhanced matrix fracture transmission conditions. 2017. hal-01518930v1

HAL Id: hal-01518930

<https://hal.science/hal-01518930v1>

Preprint submitted on 5 May 2017 (v1), last revised 9 Nov 2017 (v2)

HAL is a multi-disciplinary open access archive for the deposit and dissemination of scientific research documents, whether they are published or not. The documents may come from teaching and research institutions in France or abroad, or from public or private research centers.

L'archive ouverte pluridisciplinaire **HAL**, est destinée au dépôt et à la diffusion de documents scientifiques de niveau recherche, publiés ou non, émanant des établissements d'enseignement et de recherche français ou étrangers, des laboratoires publics ou privés.

Hybrid-dimensional modelling of two-phase flow through fractured porous media with enhanced matrix fracture transmission conditions

K. Brenner*, J. Hennicker*[†], R. Masson*, P. Samier[†]

May 5, 2017

Abstract

In this work, we extend the single-phase Darcy flow model proposed in [25], [12] to two-phase flow. We propose two models for two-phase Darcy flow through fracture networks in porous media, in which the $(d - 1)$ -dimensional flow in the fractures is coupled with the d -dimensional flow in the matrix, leading to the so called hybrid-dimensional Darcy flow models. They both account for fractures acting either as drains or as barriers, since they allow pressure jumps at the matrix-fracture interfaces. The models also permits to treat gravity dominated flow as well as discontinuous capillary pressure at the material interfaces. We adapt the Vertex Approximate Gradient (VAG) scheme to this problem, in order to account for anisotropy and heterogeneity aspects as well as for applicability on general meshes. Several test cases are presented to compare our hybrid-dimensional models to the hybrid-dimensional, continuous pressure model (proposed in [9]) and to the generic equi-dimensional model, in which fractures have the same dimension as the matrix. This does not only provide quantitative evidence about computational gain, but also leads to deep insight about the quality of the proposed reduced models.

1 Introduction

This work has two aims: providing reduced models for two-phase flows in porous media with complex Discrete Fracture Networks (DFN) and validating the reduced models by comparing them to the full (non reduced) model. More precisely, we are concerned with the modelling and the discretization of two-phase Darcy flows in fractured porous media, for which the fractures are represented as interfaces of codimension one. In this framework, the $(d - 1)$ -dimensional flow in the fractures is coupled with the d -dimensional flow in the matrix leading to the so called, hybrid-dimensional Darcy flow models. These models are derived from the so called equi-dimensional model, where fractures are represented as geological structures of equal dimension as the matrix, by averaging fracture quantities over the fracture width. We consider the case for which the pressure can be discontinuous at the matrix-fracture (mf) interfaces in order to account for fractures acting either as drains or as barriers as described in [18, 25, 6, 12], contrary to the continuous pressure model described in [3, 11] developed for conductive fractures. A hybrid-dimensional discontinuous pressure model for two-phase flow in global pressure formulation has been derived in [26, 2]. In order to account more efficiently for discontinuous capillary pressures, our models use the phase pressures as primary unknowns. This formulation is based on the inverse of the monotone graph extension of the capillary pressure curves and can be easily extended to general capillary pressure curves including vanishing capillary pressures in the fracture using a switch of variable formulation as described in [10]. Our coupling conditions at the mf interfaces also differ from the ones presented in [26, 2] in the sense that they incorporate an upwinding between the matrix and fracture mobilities and do not neglect the gravitational force. This upwinding is crucial in order to transport fluid from the matrix to the fractures and the gravitational force in the

*Laboratoire de Mathématiques J.A. Dieudonné, UMR 7351 CNRS, University Nice Sophia Antipolis, and team COFFEE, INRIA Sophia Antipolis Méditerranée, Parc Valrose 06108 Nice Cedex 02, France, {konstantin.brenner, julian.hennicker, roland.masson}@unice.fr

[†]CSTJF, TOTAL S.A. - Avenue Larribau, 64018 Pau, France

width of the fracture cannot be neglected for gravity dominant flows independently on the fracture width. The discontinuous hybrid-dimensional model, presented in section 2.2 is based on the two-phase Darcy flux continuity at the mf interfaces. At the discrete level, we propose a modification of this model in section 3.3, which still accounts for pressure discontinuities at the mf interfaces, but provides linear matrix-fracture transmission conditions. Subsequently, in a series of test cases, we compare the discontinuous hybrid-dimensional models with the equi-dimensional model and with the hybrid-dimensional model presented in [9] and which assumes pressure continuity across the fractures accounting only for conductive fractures.

The discretization of hybrid-dimensional Darcy flow models has been the object of several works. For an exhaustive review of existing methods, we refer to [30, 32]. For single-phase Darcy flow, a cell-centered Finite Volume scheme using a Two Point Flux Approximation (TPFA) is proposed in [18, 6] assuming the orthogonality of the mesh and isotropic permeability fields. Cell-centered Finite Volume schemes using MultiPoint Flux Approximations (MPFA) have been studied in [33, 31, 1]. In [25], a Mixed Finite Element (MFE) method is proposed. Let us also mention two classes of so-called geometrically non-conforming discretizations, that handle non-matching fracture and matrix meshes: the Extended Finite Element Method [5, 19, 20] and the Embedded Discrete Fracture Method [27, 22]. More recently the Hybrid Finite Volume (HFV) scheme, introduced in [15], has been extended in [17] for the geometrically non-conforming discretization of two reduced fault models. Also a Mimetic Finite Difference (MFD) scheme is used in [7] in the matrix domain coupled with a TPFA scheme in the fracture network. Discretizations of the related reduced model [3] assuming a continuous pressure at the matrix fracture interfaces have been proposed in [3] using a MFE method and in [11] using the HFV scheme and an extension of the Vertex Approximate Gradient (VAG) scheme introduced in [14]. Finally, the VAG and HFV schemes have been extended to the single-phase hybrid-dimensional discontinuous pressure model in [12]. For two-phase Darcy flow, a cell-centred Finite Volume scheme using a Two Point Flux Approximation (TPFA) is proposed in [24], assuming the orthogonality of the mesh and isotropic permeability fields. Cell-centred Finite Volume schemes can be extended to general meshes and anisotropic permeability fields using MultiPoint Flux Approximations (MPFA) following the ideas introduced in [33] for discontinuous pressure models. Nevertheless, MPFA schemes can lack robustness on distorted meshes and large anisotropies due to the non symmetry of the discretization. They are also very expensive compared to nodal discretizations on tetrahedral meshes. In [23], the two-phase flow equations are solved in an IMPES framework, using a Mixed Hybrid Finite Element (MHFE) discretization for the pressure equation and a Discontinuous Galerkin discretization of the saturation equation. The paper also contains a review on the most common numerical approaches, when dealing with discrete fractures. The Hybrid Finite Volume discretization (HFV, see [15]) is extended to two phase Darcy flow in fractured media in [21]. These approaches are adapted to general meshes and anisotropy but require as many degrees of freedom as faces. An early paper to use a Control Volume Finite Element method (CVFE) for the discretization of hybrid-dimensional two-phase flow is [8]. In [29], a CVFE scheme is proposed that use reconstruction operators for the saturations that depend on the rock characteristic capillary pressure curves. In this way, the saturation jumps (due to discontinuous capillary pressure) at the material interfaces are respected. A similar approach can be found in [28] in phase pressure formulation. However, the rigid choice of the control volumes (that are the dual cells) leads to the need of small matrix cells at the DFN neighbourhood, in order not to enlarge the drain artificially. In [9], the VAG scheme is used, which is very flexible in the distribution of control volumes and hence circumvents this problem. To the author's knowledge, there has not yet appeared a comparison of different hybrid-dimensional models with the generic equi-dimensional model for two-phase flow. This is one of the achievements of the present paper.

In this work, we present an adaptation of the VAG scheme to the hybrid-dimensional discontinuous pressure model using supplementary unknowns at the mf interfaces to capture the pressure jumps as initially proposed in [12]. We choose a vertex based scheme, because it leads, compared to the cell-centered and face-centered approaches, to a smaller number of degrees of freedom when dealing with symplectic meshes, which in turn often arise when complex geometries have to be taken into account. Furthermore, the control volume version of the VAG scheme, presented here, allows to take

into account saturation jumps (due to capillary pressure) at rock type interfaces including the mf interfaces. An important novelty of the proposed scheme is that the saturations at the interfacial unknowns are explicitly calculated, in addition to the saturations inside the fractures. All of the aforementioned schemes lack in this supplementary information. They either have just one unknown at the fractures, which is the case for the hybrid dimensional continuous pressure models, or they eliminate the interfacial unknowns at the linear level. The importance of preserving the information on interfacial and interior saturations at the fractures becomes obvious in the test case section of this work: the influence on the solution of capillary or gravitational forces in normal direction within the fractures is far from being negligible, in general. The supplementary unknowns at the mf interfaces enable the method presented in this paper to capture these effects.

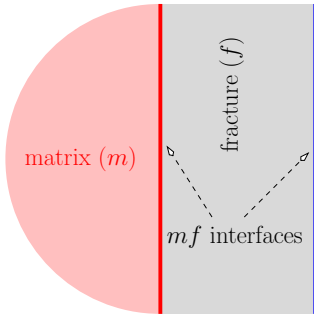


Figure 1: Nomenclature.

The outline of this work is as follows. The hybrid-dimensional two-phase flow models are provided in section 2. Section 3 is devoted to the VAG discretization and provides a finite volume formulation of the models. In section 4, the hybrid and equi-dimensional models are compared on a tracer problem with analytical solutions. The effect of a normal diffusion term in the fracture for the equi-dimensional model is also investigated. The last section 5 compares the three hybrid-dimensional models with the equi-dimensional model on a two-phase flow problem with different matrix and fracture permeabilities and capillary pressures.

2 Hybrid-dimensional Modelling of Flow in Fractured Porous Media

Fractures and faults are geological structures with highly contrasted petro- and hydrological properties and a small thickness compared to the surrounding matrix. To derive the hybrid-dimensional model, we average the continuity and Darcy equations over the fracture width. The main objectives are to facilitate mesh generation and to decrease the number of degrees of freedom involved in the numerical resolution of the corresponding discrete problem.

2.1 Discrete Fracture Network

Let Ω denote a bounded domain of \mathbb{R}^d , $d = 2, 3$ assumed to be polyhedral for $d = 3$ and polygonal for $d = 2$. To fix ideas the dimension will be set to $d = 3$ when it needs to be specified, for instance in the naming of the geometrical objects or for the space discretization in the next section. The adaptations to the case $d = 2$ are straightforward.

Let $\bar{\Gamma} = \bigcup_{i \in I} \bar{\Gamma}_i$ and its interior $\Gamma = \bar{\Gamma} \setminus \partial \bar{\Gamma}$ denote the network of fractures $\Gamma_i \subset \Omega$, $i \in I$, which is a collection of planar polygonal simply connected open domains, such that each Γ_i is included in a plane \mathcal{P}_i of \mathbb{R}^d . Without loss of generality, we will assume that the angles of Γ_i are strictly smaller than 2π , and that $\Gamma_i \cap \bar{\Gamma}_j = \emptyset$ for all $i \neq j$. For all $i \in I$, let us set $\Sigma_i = \partial \Gamma_i$, with \mathbf{n}_{Σ_i} as unit vector in \mathcal{P}_i , normal to Σ_i and outward to Γ_i . Further $\Sigma_{i,j} = \Sigma_i \cap \Sigma_j$, $j \in I \setminus \{i\}$, $\Sigma_{i,0} = \Sigma_i \cap \partial \Omega$, $\Sigma_{i,N} = \Sigma_i \setminus (\bigcup_{j \in I \setminus \{i\}} \Sigma_{i,j} \cup \Sigma_{i,0})$, $\Sigma = \bigcup_{(i,j) \in I \times I, i \neq j} (\Sigma_{i,j} \setminus \Sigma_{i,0})$ and $\Sigma_0 = \bigcup_{i \in I} \Sigma_{i,0}$.

We define the two unit normal vectors $\mathbf{n}_{\mathbf{a}^\pm(i)}$ at each planar fracture Γ_i , such that $\mathbf{n}_{\mathbf{a}^+(i)} + \mathbf{n}_{\mathbf{a}^-(i)} = 0$ (cf. figure 2). We define the set of indices $\chi = \{\mathbf{a}^+(i), \mathbf{a}^-(i) \mid i \in I\}$, such that $\#\chi = 2\#I$. For ease of notation, we use the convention $\Gamma_{\mathbf{a}^+(i)} = \Gamma_{\mathbf{a}^-(i)} = \Gamma_i$. Then, for $\mathbf{a} = \mathbf{a}^\pm(i) \in \chi$, we can define the trace operator on $\Gamma_{\mathbf{a}}$:

$$\gamma_{\mathbf{a}} : H^1(\Omega \setminus \bar{\Gamma}) \rightarrow L^2(\Gamma_{\mathbf{a}}),$$

and the normal trace operator on $\Gamma_{\mathbf{a}}$ outward to the side \mathbf{a} :

$$\gamma_{\mathbf{n}_{\mathbf{a}}} : H_{\text{div}}(\Omega \setminus \bar{\Gamma}) \rightarrow \mathcal{D}'(\Gamma_{\mathbf{a}}),$$

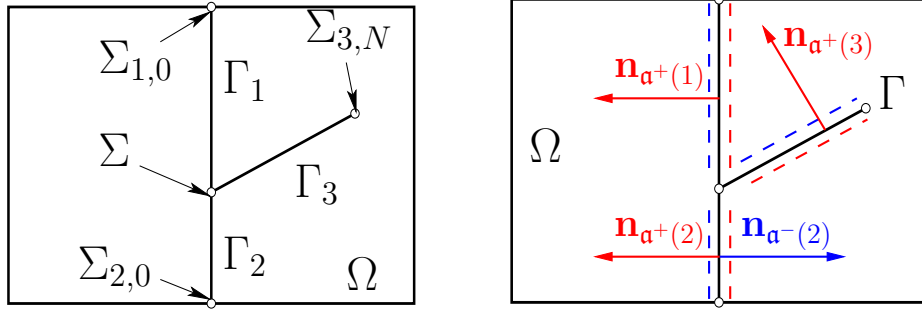


Figure 2: Example of a 2D domain Ω and 3 intersecting fractures $\Gamma_i, i = 1, 2, 3$. We define the fracture plane orientations by $\mathbf{a}^\pm(i) \in \chi$ for $\Gamma_i, i \in I$.

that satisfy $\gamma_{\mathbf{a}}(h) = \gamma_{\Gamma_i}(h|_{\omega_{\mathbf{a}}})$ and $\gamma_{\mathbf{n}_{\mathbf{a}}}(\mathbf{p}) = \gamma_{\mathbf{n}, \Gamma_i}(\mathbf{p}|_{\omega_{\mathbf{a}}})$, where $\omega_{\mathbf{a}} = \{\mathbf{x} \in \Omega \mid (\mathbf{x} - \mathbf{y}) \cdot \mathbf{n}_{\mathbf{a}} < 0, \forall \mathbf{y} \in \Gamma_i\}$, and where γ_{Γ_i} and $\gamma_{\mathbf{n}, \Gamma_i}$ are the usual trace and normal trace operators defined of $H^1(\omega_{\mathbf{a}})$ and $H_{\text{div}}(\omega_{\mathbf{a}})$ respectively.

2.2 Two-phase Darcy flow models

Equi-dimensional model. We consider the flow equations for incompressible, immiscible two-phase flow on a d -dimensional porous domain Ω containing a fracture Ω_f as illustrated in figure 3. To simplify, we consider no sources or sinks.

$$\phi \partial_t S^\alpha(\mathbf{x}, p) + \text{div}(\mathbf{q}^\alpha) = 0, \quad (1a)$$

$$\mathbf{q}^\alpha = -k^\alpha(\mathbf{x}, S^\alpha(\mathbf{x}, p)) \Lambda(\nabla u^\alpha - \rho^\alpha \mathbf{g}), \quad (1b)$$

with phase parameter $\alpha \in \{1, 2\}$ (1 for a non wetting phase and 2 for a wetting phase), phase pressures u^α , phase Darcy velocities \mathbf{q}^α , capillary pressure p , phase saturations S^α , permeability tensor Λ (positive definite), porosity ϕ , phase mobility k^α phase mass densities ρ^α gravitational vector field \mathbf{g} and space coordinate $\mathbf{x} \in \Omega$. The system is closed by the equations

$$p = u^1 - u^2, \quad S^1(\mathbf{x}, p) + S^2(\mathbf{x}, p) = 1. \quad (1c)$$

Model (1) will be referred to as the equi-dimensional model, in the following.

Derivation of the hybrid-dimensional models. We suppose that the matrix and the fracture network consist of a finite number of geological formations, that define finite partitions of $\Omega \setminus \Omega_f$ and Ω_f . To identify those geological formations mathematically, we attribute a proper rock type rt to each open set ω_{rt} of these partitions. Then, we assume that on each ω_{rt} , k^α and S^α are not explicitly space dependent. Moreover, on ω_{rt} , $S^1(q) \in [0, 1]$ for all $q \in \mathbb{R}$ and S^1 is a non decreasing continuous function on \mathbb{R} , and k^α is a continuous, non-negative valued function on $[0, 1]$, for $\alpha = 1, 2$.

The fracture has the representation $\Omega_f = \{\mathbf{x} \in \Omega \mid \mathbf{x} = \mathbf{y} + r\mathbf{n}(\mathbf{y}), \mathbf{y} \in \Gamma, r \in (-\frac{d_f(\mathbf{y})}{2}, \frac{d_f(\mathbf{y})}{2})\}$, where \mathbf{n} is a unit normal vector and d_f is the fracture width. Let us further introduce the orthonormal system of tangential vectors $(\boldsymbol{\tau}_1, \dots, \boldsymbol{\tau}_{d-1})$ on Γ and the corresponding tangential divergence div_τ and gradient ∇_τ . We assume that inside the fractures, the normal direction is a permeability principal direction, such that the permeability tensor decomposes in a tangential part and a normal part as

$$\Lambda = \Lambda_f + \lambda_{f,n} \mathbf{n} \otimes \mathbf{n}, \quad (2)$$

with $\Lambda_f \mathbf{n} = 0$. On Ω_f , we also assume that the permeability and porosity, as well as the constitutive relations for the phase saturations and mobilities do not explicitly depend on the normal component of the spacial coordinate (we will use the index f to denote their projections on Γ).

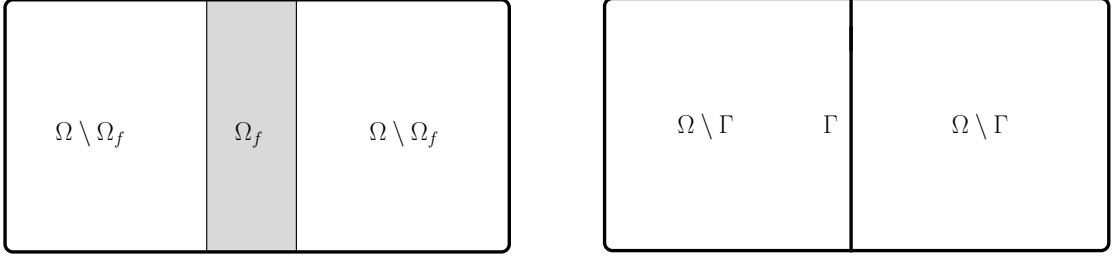


Figure 3: Geometries of the equi-dimensional model (left) and the hybrid-dimensional model (right) in the case of a single fracture dividing the matrix domain.

To start, we write

$$\mathbf{q}^\alpha = \sum_{i=1}^{d-1} (\mathbf{q}^\alpha \cdot \boldsymbol{\tau}_i) \boldsymbol{\tau}_i + (\mathbf{q}^\alpha \cdot \mathbf{n}) \mathbf{n}. \quad (3)$$

Let $\mathbf{g}_\tau = \mathbf{g} - (\mathbf{g} \cdot \mathbf{n}) \mathbf{n}$. With (2) and (3), (1b) is equivalent to

$$\sum_{i=1}^{d-1} (\mathbf{q}^\alpha \cdot \boldsymbol{\tau}_i) \boldsymbol{\tau}_i = -k_f^\alpha(\mathbf{x}, S_f^\alpha(\mathbf{x}, p)) \Lambda_f (\nabla_\tau u^\alpha - \rho^\alpha \mathbf{g}_\tau) \quad (4a)$$

$$\mathbf{q}^\alpha \cdot \mathbf{n} = -k_f^\alpha(\mathbf{x}, S_f^\alpha(\mathbf{x}, p)) \lambda_{f,n} (\partial_n u^\alpha - \rho^\alpha \mathbf{g} \cdot \mathbf{n}). \quad (4b)$$

Respectively, the averaged pressure and the integrated tangential Darcy velocity across the fracture are defined by

$$u_f^\alpha = \frac{1}{d_f} \int_{-\frac{d_f}{2}}^{\frac{d_f}{2}} u^\alpha \, \mathrm{d}\mathbf{n} \quad \text{and} \quad \mathbf{q}_f^\alpha = \sum_{i=1}^{d-1} \int_{-\frac{d_f}{2}}^{\frac{d_f}{2}} (\mathbf{q}^\alpha \cdot \boldsymbol{\tau}_i) \boldsymbol{\tau}_i \, \mathrm{d}\mathbf{n}.$$

Furthermore, let us use the approximations

$$k_f^\alpha(\mathbf{x}, S_f^\alpha(\mathbf{x}, p)) \approx k_f^\alpha(\mathbf{x}, S_f^\alpha(\mathbf{x}, p_f)) \quad \text{and} \quad S_f^\alpha(\mathbf{x}, p_f) \approx \frac{1}{d_f} \int_{-\frac{d_f}{2}}^{\frac{d_f}{2}} S_f^\alpha(\mathbf{x}, p) \, \mathrm{d}\mathbf{n}.$$

Integration of the conservation equation (1a) and the tangential Darcy law (4a) over the fracture width yields the fracture equations for the hybrid-dimensional model,

$$\begin{cases} \phi_f d_f \partial_t S_f^\alpha(\mathbf{x}, p_f) + \operatorname{div}_\tau(\mathbf{q}_f^\alpha) - \sum_{\mathbf{a} \in \chi} \gamma_{\mathbf{n}_a} \mathbf{q}_m^\alpha = 0 & \text{on } \Gamma \\ \mathbf{q}_f^\alpha = -d_f k_f^\alpha(\mathbf{x}, S_f^\alpha(\mathbf{x}, p_f)) \Lambda_f (\nabla_\tau u_f - \rho^\alpha \mathbf{g}_\tau) & \text{on } \Gamma \end{cases} \quad (5a)$$

The matrix equations for the hybrid-dimensional model are

$$\begin{cases} \phi_m \partial_t S_m^\alpha(\mathbf{x}, p_m) + \operatorname{div}(\mathbf{q}_m^\alpha) = 0 & \text{on } \Omega \setminus \bar{\Gamma} \\ \mathbf{q}_m^\alpha = -k_m^\alpha(\mathbf{x}, S_m^\alpha(\mathbf{x}, p_m)) \Lambda_m (\nabla u_m^\alpha - \rho^\alpha \mathbf{g}) & \text{on } \Omega \setminus \bar{\Gamma} \end{cases} \quad (5b)$$

Moreover, both phases are coupled by the equations

$$(p_m, p_f) = (u_m^1 - u_m^2, u_f^1 - u_f^2), \quad (S_m^2, S_f^2) = 1 - (S_m^1, S_f^1). \quad (5c)$$

Discontinuous hybrid-dimensional model. The matrix and the fracture equations are coupled by Robin boundary conditions imposed at each $\Gamma_{\mathbf{a}}$, $\mathbf{a} \in \chi$. For this, we use a two point approximation of the normal derivative of the pressure in the linear part of (4b), which leads to the definition of the velocity

$$V_{f,n}^{\alpha,\mathbf{a}} = \lambda_{f,n} \left(\frac{\gamma_{\mathbf{a}} u_m^\alpha - u_f^\alpha}{d_f/2} - \rho^\alpha \gamma_{\mathbf{a}} \mathbf{g} \right). \quad (6)$$

In order to transport the saturations between the matrix and the fractures, the mobility has to be upwinded in the definition of the normal flux $\gamma_{\mathbf{n}_a} \mathbf{q}_m^\alpha$. For any $a \in \mathbb{R}$, let us set $a^+ = \max\{0, a\}$ and $a^- = -(-a)^+$. The resulting equation on $\Gamma_{\mathbf{a}}$, $\mathbf{a} \in \chi$ is

$$\begin{aligned} \gamma_{\mathbf{n}_a} \mathbf{q}_m^\alpha &= \mathbf{q}_{f,\mathbf{n}_a}^\alpha \\ \mathbf{q}_{f,\mathbf{n}_a}^\alpha &= k_f^\alpha(\mathbf{x}, S_f^\alpha(\mathbf{x}, \gamma_{\mathbf{a}} p_m)) (V_{f,n}^{\alpha,\mathbf{a}})^+ + k_f^\alpha(\mathbf{x}, S_f^\alpha(\mathbf{x}, p_f)) (V_{f,n}^{\alpha,\mathbf{a}})^-. \end{aligned} \quad (7)$$

As illustrated in figure 4, the upwinding of the mobilities in the definition of the flux $\mathbf{q}_{f,\mathbf{n}_a}^\alpha$ takes into account the saturation jump due to discontinuous capillary pressure curves at the matrix-fracture interface.

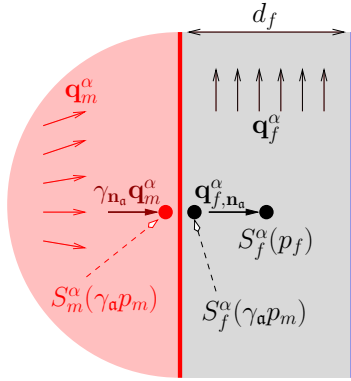


Figure 4: Illustration of the coupling condition $\mathbf{q}_{f,\mathbf{n}_a}^\alpha = \gamma_{\mathbf{n}_a} \mathbf{q}_m^\alpha$ for the discontinuous hybrid-dimensional model.

Model (5),(7) will be referred to as the type hybrid-dimensional model accounting for pressure discontinuities at the matrix-fracture interfaces, or shortly, the discontinuous hybrid-dimensional model.

Continuous hybrid-dimensional model. When $\frac{\lambda_{f,n}}{d_f} \gg \frac{|\Lambda_m|}{\text{diam}(\Omega)}$, condition (6) can be further approximated by the pressure continuity condition at the matrix fracture interface Γ

$$\gamma_{\mathbf{a}^+(i)} u_m^\alpha = \gamma_{\mathbf{a}^-(i)} u_m^\alpha = u_f, \quad (8)$$

recovering the condition introduced in [3] for single-phase Darcy flows and in [8, 29, 9] for two-phase flows. The model defined by (5),(8) will be referred to as the continuous hybrid-dimensional model, in the rest of this paper.

DFN closure conditions. Finally, closure conditions are set at the immersed boundary of the fracture network (fracture tips) as well as at the intersection between fractures. For $i \in I$, let γ_{Σ_i} (resp. $\gamma_{\mathbf{n}_{\Sigma_i}}$) denote the trace (resp. normal trace) operator at the fracture Γ_i boundary oriented outward to Γ_i , and let $\gamma_{\mathbf{n}_{\partial\Gamma}}$ denote the normal trace operator at the fracture network boundary oriented outward to Γ . At fracture tips $\partial\Gamma \setminus \partial\Omega$, it is classical to assume homogeneous Neumann boundary conditions in the sense that

$$\gamma_{\mathbf{n}_{\partial\Gamma}} \mathbf{q}_f^\alpha = 0 \quad \text{on } \partial\Gamma \setminus \partial\Omega, \quad \alpha = 1, 2,$$

meaning that the flow at the tip of a fracture can be neglected compared with the flow along the sides of the fracture. At the fracture intersection $\Sigma_{i,j} \setminus \Sigma_{i,0}$, $i, j \in I, i \neq j$, we impose the normal flux conservation equations

$$\sum_{k \in I} \gamma_{\mathbf{n}_{\Sigma_k}} \mathbf{q}_f^\alpha = 0 \quad \text{on } \Sigma_{i,j} \setminus \Sigma_{i,0}, \quad \alpha = 1, 2,$$

meaning that the volume at the intersection between fractures is neglected. In addition, we impose continuity of the phase pressures at $\Sigma_{i,j}$

$$\gamma_{\Sigma_i} u_f^\alpha = \gamma_{\Sigma_j} u_f^\alpha \quad \text{on } \Sigma_{i,j}, \quad \alpha = 1, 2.$$

This amounts to assume a high ratio between the permeability at the intersection and the fracture width compared with the ratio between the tangential permeability of each fracture and its length.

Up to now, the only existing, comparable hybrid-dimensional two-phase flow model to the discontinuous hybrid-dimensional model presented above is the model described in [2, 26], which is presented in global pressure formulation. We adapted here a formulation using the phase pressures as primary unknowns, accounting for complex fracture networks and general invertible capillary pressure functions. As illustrated in the numerical section it can be easily extended to general capillary pressure curves including vanishing capillary pressure in the fractures using a switch of variable formulation as described in [10].

Another difference is, that the discontinuous hybrid-dimensional model uses an upwind coupling condition for the matrix-fracture normal fluxes (see (7)). This upwinding is necessary to transport the saturations from the matrix to the fractures. The coupling condition (7) also takes into account gravitational force inside the fractures for the matrix-fracture mass exchange. In the test cases below, we see that this is an important feature for the simulation of gravity dominant flow.

3 Vertex Approximate Gradient Scheme

In this section, the VAG scheme, introduced in [14] for diffusive problems on heterogeneous anisotropic media and extended to discrete fractures in [11] for the continuous and in [12] for the discontinuous hybrid dimensional models, is adapted to the hybrid-dimensional two-phase flow models. We consider a finite volume version using lumping both for the accumulation terms and the matrix fracture fluxes.

3.1 VAG Discretization

3.1.1 Polyhedral meshes

Following [14], we consider generalized polyhedral meshes of Ω . Let \mathcal{M} be the set of cells that are disjoint open polyhedral subsets of Ω such that $\bigcup_{K \in \mathcal{M}} \bar{K} = \bar{\Omega}$. For all $K \in \mathcal{M}$, \mathbf{x}_K denotes the so-called ‘‘center’’ of the cell K under the assumption that K is star-shaped with respect to \mathbf{x}_K . Let \mathcal{F} denote the set of (not necessarily planar) faces of the mesh. We denote by \mathcal{V} the set of vertices of the mesh. Let \mathcal{V}_K , \mathcal{F}_K , \mathcal{V}_σ respectively denote the set of the vertices of $K \in \mathcal{M}$, faces of K , and vertices of $\sigma \in \mathcal{F}$. For any face $\sigma \in \mathcal{F}_K$, we have $\mathcal{V}_\sigma \subset \mathcal{V}_K$. Let \mathcal{M}_s (resp. \mathcal{F}_s) denote the set of the cells (resp. faces) sharing the vertex $s \in \mathcal{V}$. The set of edges of the mesh is denoted by \mathcal{E} and \mathcal{E}_σ denotes the set of edges of the face $\sigma \in \mathcal{F}$. Let \mathcal{M}_σ denote the set of cells sharing the face $\sigma \in \mathcal{F}$. We denote by \mathcal{F}_{ext} the subset of faces $\sigma \in \mathcal{F}$ such that \mathcal{M}_σ has only one element, and we set $\mathcal{V}_{ext} = \bigcup_{\sigma \in \mathcal{F}_{ext}} \mathcal{V}_\sigma$. The mesh is assumed to be conforming in the sense that for all $\sigma \in \mathcal{F} \setminus \mathcal{F}_{ext}$, the set \mathcal{M}_σ contains exactly two cells. It is assumed that for each face $\sigma \in \mathcal{F}$, there exists a so-called ‘‘center’’ of the face \mathbf{x}_σ such that

$$\mathbf{x}_\sigma = \sum_{s \in \mathcal{V}_\sigma} \beta_{\sigma,s} \mathbf{x}_s, \quad \text{with} \quad \sum_{s \in \mathcal{V}_\sigma} \beta_{\sigma,s} = 1,$$

where $\beta_{\sigma,s} \geq 0$ for all $s \in \mathcal{V}_\sigma$. The face σ is assumed to match with the union of the triangles $T_{\sigma,e}$ defined by the face center \mathbf{x}_σ and each of its edges $e \in \mathcal{E}_\sigma$. The mesh is assumed to be conforming w.r.t. the fracture network Γ in the sense that there exist subsets \mathcal{F}_{Γ_i} , $i \in I$ of \mathcal{F} such that

$$\bar{\Gamma}_i = \bigcup_{\sigma \in \mathcal{F}_{\Gamma_i}} \bar{\sigma}.$$

We will denote by \mathcal{F}_Γ the set of fracture faces $\bigcup_{i \in I} \mathcal{F}_{\Gamma_i}$. Similarly, we will denote by \mathcal{V}_Γ the set of fracture vertices $\bigcup_{\sigma \in \mathcal{F}_\Gamma} \mathcal{V}_\sigma$. We also define a submesh \mathcal{T} of tetrahedra, where each tetrahedron $D_{K,\sigma,e}$

is the convex hull of the cell center \mathbf{x}_K of K , the face center \mathbf{x}_σ of $\sigma \in \mathcal{F}_K$ and the edge $e \in \mathcal{E}_\sigma$. Similarly we define a triangulation Δ of Γ , such that we have:

$$\mathcal{T} = \bigcup_{K \in \mathcal{F}, \sigma \in \mathcal{F}_K, e \in \mathcal{E}_\sigma} \{D_{K,\sigma,e}\} \quad \text{and} \quad \Delta = \bigcup_{\sigma \in \mathcal{F}_\Gamma, e \in \mathcal{E}_\sigma} \{T_{\sigma,e}\}.$$

The mesh is also assumed to be conforming w.r.t. the rock types, in the sense that we have a well defined rock type for each cell and fracture face, denoted by rt_K and rt_σ , for $K \in \mathcal{M}$ and $\sigma \in \mathcal{F}_\Gamma$.

3.1.2 Degrees of freedom

The set of matrix and fracture degrees of freedom is denoted by $dof_{\mathcal{D}} = dof_{\mathcal{D}_m} \cup dof_{\mathcal{D}_f}$, with $dof_{\mathcal{D}_m} \cap dof_{\mathcal{D}_f} = \emptyset$. The real vector space of discrete unknowns is denoted by $X_{\mathcal{D}} = \mathbb{R}^{\#dof_{\mathcal{D}}}$. For $u_{\mathcal{D}} \in X_{\mathcal{D}}$ and $\nu \in dof_{\mathcal{D}}$, we denote by u_ν the ν th component of $u_{\mathcal{D}}$. To account for Dirichlet boundary conditions on $\partial\Omega$ and Σ_0 we introduce the subsets $dof_{Dir_m} \subset dof_{\mathcal{D}_m}$, and $dof_{Dir_f} \subset dof_{\mathcal{D}_f}$, and we set $dof_{Dir} = dof_{Dir_m} \cup dof_{Dir_f}$, and $X_{\mathcal{D}}^0 = \{u_{\mathcal{D}} \in X_{\mathcal{D}} \mid u_\nu = 0 \text{ for all } \nu \in dof_{Dir}\}$. Concretely, we consider the set of d.o.f. as illustrated in figure 5.

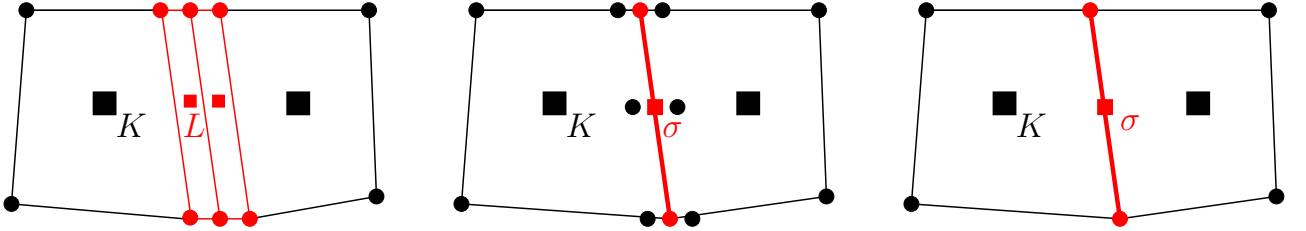


Figure 5: Illustration of d.o.f. in 2D for a matrix domain (in black) intersected by a fracture (in red) for the equi-dimensional and discontinuous and continuous hybrid-dimensional models (from left to right).

Equi-dimensional model. Since the equi-dimensional approach does not reduce the fracture dimension, we have to deal with small fracture cells. The standard VAG scheme, as introduced in [14] for single-phase flow and in [16] for multiphase flows, which is based on cell and node unknowns, is used for this model.

Discontinuous hybrid-dimensional model. The set $dof_{\mathcal{D}_f}$ of fracture d.o.f. relate to face unknowns and node unknowns. This corresponds to the d.o.f. of the standard VAG scheme in dimension $d - 1$ on the fracture network. Let us split $dof_{\mathcal{D}_m}$ in the interfacial d.o.f. $dof_{\mathcal{D}_m}^\Gamma$, located at the fracture network, and the bulk d.o.f. $dof_{\mathcal{D}_m} \setminus dof_{\mathcal{D}_m}^\Gamma$. The unknowns at the interfaces are necessary in order to capture the pressure discontinuities between the matrix and fractures. Since we have to take into account these pressure jumps for all fracture unknowns and all m_f interfaces, $dof_{\mathcal{D}_m}^\Gamma$ refers to node unknowns plus face unknowns, which are related to the fracture d.o.f. one-to-one for each side of the DFN. Most often, the fractures cut the matrix domain in two. For immersed fracture tips or multiple fracture intersections, however, we have up to as many unknowns as fractures connected to the spot (cf. figure 6). The set $dof_{\mathcal{D}_m} \setminus dof_{\mathcal{D}_m}^\Gamma$ corresponds to cell unknowns and node unknowns, which are the classical unknowns for the VAG scheme in d dimensions. We refer to [12], for a more detailed presentation.

Continuous hybrid-dimensional model. The set $dof_{\mathcal{D}}$ consisting of the model degrees of freedom, corresponds to cell, node and fracture face unknowns as illustrated in figure 5. These are the unknowns of the hybrid-dimensional models above, with the exception that $dof_{\mathcal{D}_m}^\Gamma = \emptyset$. For more details, we refer to [11].

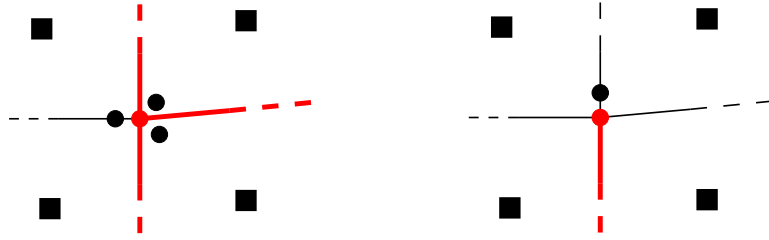


Figure 6: Zoom on the fracture intersection for three fractures (left) and on the fracture tip for one immersed fracture (right). Illustrated are four cells (indicated as boxes) and the d.o.f. at the singular point for the discontinuous hybrid-dimensional models (interfacial d.o.f. in black and fracture d.o.f. in red).

3.1.3 \mathbb{P}_1 Finite Element basis functions

The basis functions we use to discretize the diffusion terms, denoted by η_ν , $\nu \in \text{dof}_{\mathcal{D}}$, in the following, are the \mathbb{P}_1 Finite Element basis functions on the tetrahedral submesh \mathcal{T} , for $\nu \in \text{dof}_{\mathcal{D}_m}$ and on the triangulation Δ of the DFN, for $\nu \in \text{dof}_{\mathcal{D}_f}$. The discrete gradients are then defined as the \mathbb{P}_1 Finite Element gradients on each of the connected matrix subdomains and on the DFN, respectively. For the treatment of the jump terms at the matrix-fracture interfaces, the basis functions are lumped onto a dual mesh of the triangulation Δ . For a more detailed presentation of the construction of the basis functions and discrete gradients, we refer to [12], for the discontinuous and to [9] for the continuous hybrid-dimensional models. To respect the heterogeneities of the media, the VAG reconstructions of the accumulation terms are piecewise constant, as described below.

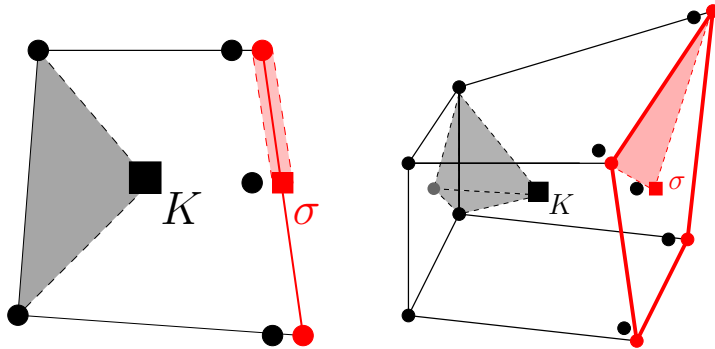


Figure 7: 2D (left) resp. 3D (right) cell K touching a fracture face σ . Illustration of the simplices on which the matrix (grey) and fracture (red) discrete gradients are constant. The facial unknown located at the coordinate in light grey is eliminated by barycentric interpolation.

3.1.4 Control volumes

As mentioned above, the mesh is conforming with the partition in rock types. So, we introduce, for any given $K \in \mathcal{M}$, a partition of K , which takes the general form $\{\omega_K^\nu\}_{\nu \in \{K\} \cup (\text{dof}_K \cap \text{dof}_{\mathcal{D}_m}) \setminus \text{dof}_{\text{Dir}}}$ and for any given $\sigma \in \mathcal{F}_\Gamma$ a partition $\{\omega_\sigma^\nu\}_{\nu \in \{\sigma\} \cup (\text{dof}_\sigma \cap \text{dof}_{\mathcal{D}_f}) \setminus \text{dof}_{\text{Dir}}}$ of σ . Here, dof_K and dof_σ stand for the d.o.f. connected to K and σ , respectively, as explained below. The VAG reconstructions of the accumulation terms are piecewise constant on these distributions, and therefore respect the heterogeneities of the media (see [13]). Integrating the reconstructed accumulations shows that, in the numerical scheme, we do not need to provide these partitions explicitly, but only have to define their corresponding volumes.

3.2 Finite Volume Formulation of the discontinuous hybrid-dimensional model

For $\nu \in \text{dof}_{\mathcal{D}}$, let us denote by $\text{dof}_\nu \subset \text{dof}_{\mathcal{D}}$ the set consisting of all ν' , such that there is a discrete flux connection between ν and ν' as illustrated in figure 8. More concretely, for the the discontinuous

hybrid-dimensional model, these sets are defined as follows. The denomination of the different types of d.o.f. (i.e. $K, \sigma, \nu_m, \nu'_m, \nu_f$) here is consistent with the notations in figure 8.

- For $K \in \mathcal{M}$: $dof_K = \{\nu_m \in dof_{\mathcal{D}_m} \setminus dof_{\mathcal{D}_m}^\Gamma \mid \mathbf{x}_{\nu_m} \in \partial K\} \cup \{\nu_m \in dof_{\mathcal{D}_m}^\Gamma \mid \mathbf{x}_{\nu_m} \in \partial K \text{ and } \nu_m \text{ refers to an interfacial unknown located on the same side of } \Gamma \text{ as } K\}$
- For $\sigma \in \mathcal{F}_\Gamma$: $dof_\sigma = \{\nu_f \in dof_{\mathcal{D}_f} \mid \mathbf{x}_{\nu_f} \in \partial\sigma\} \cup \{\nu_m \in dof_{\mathcal{D}_m}^\Gamma \mid \mathbf{x}_{\nu_m} \in \partial\sigma\}$
- For $\nu_m \in dof_{\mathcal{D}_m}^\Gamma$: $dof_{\nu_m} = \mathcal{M}_{\nu_m} \cup \{\nu_f \in dof_{\mathcal{D}_f} \mid \mathbf{x}_{\nu_f} = \mathbf{x}_{\nu_m}\}$

Since the fluxes connect exactly two unknowns, the definition of the sets dof_ν is complemented by

$$\nu' \in dof_\nu \iff \nu \in dof_{\nu'} \quad (9)$$

The well defined constitutive relations for the mobilities and saturations for each of these rock types are then denoted by $k^\alpha(rt_\nu, \cdot)$ and $S^\alpha(rt_\nu, \cdot)$, $\nu \in \mathcal{M} \cup \mathcal{F}_\Gamma$, respectively. In order to calculate the fracture mobility for the non linear matrix-fracture two point fluxes of the discontinuous hybrid-dimensional model, for nodal unknowns, we have to define fracture node rock types, in addition to cell and fracture face rock types. The fracture node rock types serve exclusively for this purpose and its introduction is consistent with our pressure continuity assumption at fracture intersections which assumes that the properties of intersecting fractures are not too contrasted.

For any $\nu \in dof_K$ the discrete *matrix-matrix*-fluxes are defined as

$$-F_{\nu K}^\alpha(u_{\mathcal{D}}^1, u_{\mathcal{D}}^2) = F_{K\nu}^\alpha(u_{\mathcal{D}}^1, u_{\mathcal{D}}^2) = k^\alpha(rt_K, S^\alpha(rt_K, p_K)) \cdot f_{K\nu}^\alpha(u_{\mathcal{D}}^\alpha)^+ + k^\alpha(rt_K, S^\alpha(rt_K, p_\nu)) \cdot f_{K\nu}^\alpha(u_{\mathcal{D}}^\alpha)^-, \quad (10)$$

where

$$-f_{\nu K}^\alpha(u_{\mathcal{D}}^\alpha) = f_{K\nu}^\alpha(u_{\mathcal{D}}^\alpha) = \sum_{\nu' \in dof_K} T_K^{\nu\nu'} (u_K^\alpha - u_{\nu'}^\alpha - \rho^\alpha(\mathbf{x}_K - \mathbf{x}_{\nu'}) \cdot \mathbf{g}),$$

with transmissivities

$$T_K^{\nu\nu'} = \int_K \Lambda_m \nabla \eta_\nu \nabla \eta_{\nu'} \, dx.$$

For all $\nu \in dof_\sigma$ the discrete *fracture-fracture*-fluxes are defined as

$$-F_{\nu\sigma}^\alpha(u_{\mathcal{D}}^1, u_{\mathcal{D}}^2) = F_{\sigma\nu}^\alpha(u_{\mathcal{D}}^1, u_{\mathcal{D}}^2) = k^\alpha(rt_\sigma, S^\alpha(rt_\sigma, p_\sigma)) \cdot f_{\sigma\nu}^\alpha(u_{\mathcal{D}}^\alpha)^+ + k^\alpha(rt_\sigma, S^\alpha(rt_\sigma, p_\nu)) \cdot f_{\sigma\nu}^\alpha(u_{\mathcal{D}}^\alpha)^-,$$

where

$$-f_{\nu\sigma}^\alpha(u_{\mathcal{D}}^\alpha) = f_{\sigma\nu}^\alpha(u_{\mathcal{D}}^\alpha) = \sum_{\nu' \in dof_\sigma} T_\sigma^{\nu\nu'} (u_\sigma^\alpha - u_{\nu'}^\alpha - \rho^\alpha(\mathbf{x}_\sigma - \mathbf{x}_{\nu'}) \cdot \mathbf{g}),$$

with transmissivities

$$T_\sigma^{\nu\nu'} = \int_\sigma d_f \Lambda_f \nabla_\tau \eta_\nu \nabla_\tau \eta_{\nu'} \, d\tau(\mathbf{x}).$$

Let us further introduce the set of *matrix-fracture* (*mf*) connectivities

$$\mathcal{C} = \{(\nu_m, \nu_f) \mid \nu_m \in dof_{\mathcal{D}_m}^\Gamma, \nu_f \in dof_{\mathcal{D}_f} \text{ s.t. } \mathbf{x}_{\nu_m} = \mathbf{x}_{\nu_f}\}.$$

The *mf*-fluxes are defined as

$$-F_{\nu_f \nu_m}^\alpha(u_{\mathcal{D}}^1, u_{\mathcal{D}}^2) = F_{\nu_m \nu_f}^\alpha(u_{\mathcal{D}}^1, u_{\mathcal{D}}^2) = k^\alpha(rt_{\nu_f}, S^\alpha(rt_{\nu_f}, p_{\nu_m})) \cdot f_{\nu_m \nu_f}^\alpha(u_{\mathcal{D}}^\alpha)^+ + k^\alpha(rt_{\nu_f}, S^\alpha(rt_{\nu_f}, p_{\nu_f})) \cdot f_{\nu_m \nu_f}^\alpha(u_{\mathcal{D}}^\alpha)^-, \quad (11)$$

where

$$-f_{\nu_f \nu_m}^\alpha(u_{\mathcal{D}}^\alpha) = f_{\nu_m \nu_f}^\alpha(u_{\mathcal{D}}^\alpha) = T_{\nu_m \nu_f} (u_{\nu_m}^\alpha - u_{\nu_f}^\alpha - \frac{\rho^\alpha d_f}{2} \gamma_{\mathbf{n}_a} \mathbf{g}),$$

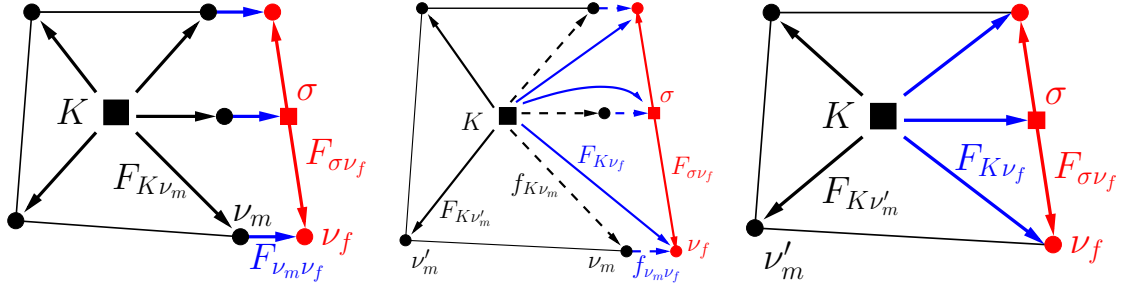


Figure 8: VAG mm -fluxes (black), mf -fluxes (blue) and ff -fluxes (red) on a 2D cell touching a fracture. Discontinuous hybrid-dimensional models 1 and 2 and continuous hybrid-dimensional model (from left to right). The fluxes indicated by solid lines and capital F correspond to non linear fluxes incorporating the mobility and appear in the flux conservation equations of each of the two control volumes they connect. The dashed fluxes f for the model 2, are linearly depending on the pressure. Consequently, the equations for interfacial $\nu_m \in \text{dof}_{\mathcal{D}_m}^\Gamma$ are the linear flux conservation equations (14), for this model.

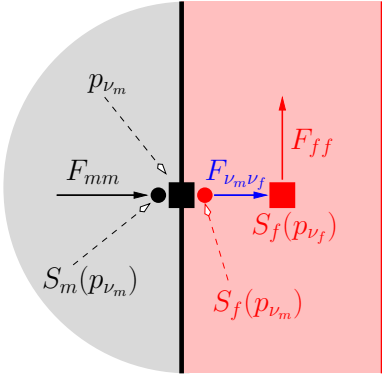


Figure 9: Model 1. Sketch of how VAG accounts for saturation jumps at the mf interfaces. The interfacial unknown is indicated by the black box and the fracture unknown by the red box. The capillary pressure p_{ν_m} for the interfacial unknown is well defined, which allows to calculate the matrix and fracture saturations at the interface, $S_m(p_{\nu_m})$ and $S_f(p_{\nu_m})$, respectively, as the inverse of the matrix and fracture capillary pressure curves. F_{mm} is calculated with $S_m(p_{\nu_m})$ and $F_{\nu_m \nu_f}$ is calculated with $S_f(p_{\nu_m})$.

with transmissivities

$$T_{\nu_m \nu_f} = \sum_{T \in \Delta} \frac{1}{3} \int_T \frac{2\lambda_{f,n}}{d_f} d\tau(\mathbf{x}).$$

s.t. $\mathbf{x}_{\nu_f} \in \bar{T}$

We observe that for the VAG scheme, the fluxes $F_{\nu_m \nu_f}^\alpha$ are two point flux approximations.

Let $0 = t^0 < t^1 < \dots < t^N = T$, with $\Delta t^n = t^n - t^{n-1}$ be a time discretization. Given $p_{\mathcal{D}}^0 \in X_{\mathcal{D}}$, and using an implicit Euler time integration, the Finite Volume formulation of (5),(7) reads as follows:

Find $\{u_{\mathcal{D}}^{\alpha}\}_{\alpha=1,2} \in (X_{\mathcal{D}}^0)^{2N}$ such that for all $n \in \{1, \dots, N\}$

$$\left\{ \begin{array}{l}
 \text{for all } K \in \mathcal{M} : \\
 |\omega_K^K| \phi_K \frac{S^{\alpha}(rt_K, p_K^n) - S^{\alpha}(rt_K, p_K^{n-1})}{\Delta t^n} + \sum_{\nu \in \text{dof}_K} F_{K\nu}^{\alpha}(u_{\mathcal{D}}^{1,n}, u_{\mathcal{D}}^{2,n}) = 0 \\
 \\
 \text{for all } \nu_m \in \text{dof}_{\mathcal{D}_m} \setminus (\mathcal{M} \cup \text{dof}_{\text{Dir}_m}) : \\
 \sum_{K \in \mathcal{M}_{\nu_m}} |\omega_K^{\nu_m}| \phi_K \frac{S^{\alpha}(rt_K, p_{\nu_m}^n) - S^{\alpha}(rt_K, p_{\nu_m}^{n-1})}{\Delta t^n} + \sum_{\nu \in \text{dof}_{\nu_m}} F_{\nu_m \nu}^{\alpha}(u_{\mathcal{D}}^{1,n}, u_{\mathcal{D}}^{2,n}) = 0 \\
 \\
 \text{for all } \sigma \in \mathcal{F}_{\Gamma} : \\
 |\omega_{\sigma}^{\sigma}| \phi_{\sigma} \frac{S^{\alpha}(rt_{\sigma}, p_{\sigma}^n) - S^{\alpha}(rt_{\sigma}, p_{\sigma}^{n-1})}{\Delta t^n} + \sum_{\nu \in \text{dof}_{\sigma}} F_{\sigma \nu}^{\alpha}(u_{\mathcal{D}}^{1,n}, u_{\mathcal{D}}^{2,n}) = 0 \\
 \\
 \text{for all } \nu_f \in \text{dof}_{\mathcal{D}_f} \setminus (\mathcal{F}_{\Gamma} \cup \text{dof}_{\text{Dir}_f}) : \\
 \sum_{\sigma \in \mathcal{F}_{\Gamma, \nu_f}} |\omega_{\sigma}^{\nu_f}| \phi_{\sigma} \frac{S^{\alpha}(rt_{\sigma}, p_{\nu_f}^n) - S^{\alpha}(rt_{\sigma}, p_{\nu_f}^{n-1})}{\Delta t^n} + \sum_{\nu \in \text{dof}_{\nu_f}} F_{\nu_f \nu}^{\alpha}(u_{\mathcal{D}}^{1,n}, u_{\mathcal{D}}^{2,n}) = 0.
 \end{array} \right. \quad (12)$$

In (12), the set \mathcal{M}_{ν_m} stands for the set of indices $\{K \in \mathcal{M} \mid \nu_m \in \text{dof}_K\}$, and $\mathcal{F}_{\Gamma, \nu_f}$ stands for the set $\{\sigma \in \mathcal{F}_{\Gamma} \mid \nu_f \in \text{dof}_{\sigma}\}$. The model of this subsection will be referred to as the discontinuous hybrid-dimensional model 1, in the following.

3.3 mf -Linearization of the discontinuous hybrid-dimensional model

For practical considerations, the equations for the interfacial unknowns $\nu_m \in \text{dof}_{\mathcal{D}_m}^{\Gamma}$ are quite costly to solve, since the interfacial accumulation volumes $\bigcup_{K \in \mathcal{M}_{\nu_m}} \omega_{K, \nu_m}$ generally have to be chosen significantly smaller than the accumulation volumes at unknowns located inside the fractures. In this section, we propose a model that uses linear equations for $\nu_m \in \text{dof}_{\mathcal{D}_m}^{\Gamma}$ to calculate the phase pressures at the matrix-fracture interfaces. On the other hand, interfacial saturations are not calculated, but matrix-fracture mass transfer uses the saturations inside the fractures, instead.

As illustrated in figure 8 for the mf -linearized discontinuous hybrid-dimensional model, the non linear flux connections defined by the sets dof_{ν} are modified for $\nu \in \text{dof}_{\mathcal{D}} \setminus \text{dof}_{\mathcal{D}_m}^{\Gamma}$ as follows:

- For $K \in \mathcal{M}$: $\text{dof}_K = \{\nu \in \text{dof}_{\mathcal{D}} \setminus \text{dof}_{\mathcal{D}_m}^{\Gamma} \mid \mathbf{x}_{\nu} \in \partial K\}$
- For $\sigma \in \mathcal{F}_{\Gamma}$: $\text{dof}_{\sigma} = \{\nu_f \in \text{dof}_{\mathcal{D}_f} \mid \mathbf{x}_{\nu_f} \in \partial \sigma\} \cup \mathcal{M}_{\sigma}$

together with the relation (9) for $\nu \in \text{dof}_{\mathcal{D}} \setminus \text{dof}_{\mathcal{D}_m}^{\Gamma}$.

Let us denote by $\nu_f(\nu_m) \in \text{dof}_{\mathcal{D}_f}$ for each $\nu_m \in \text{dof}_{\mathcal{D}_m}^{\Gamma}$, the unique d.o.f. $\nu_f \in \text{dof}_{\mathcal{D}_f}$ such that $\mathbf{x}_{\nu_m} = \mathbf{x}_{\nu_f}$. Unlike for the discontinuous hybrid-dimensional model 1, the d.o.f. $\nu_m \in \text{dof}_{\mathcal{D}_m}^{\Gamma}$ are not linked to their neighbours via non linear fluxes. Also, in the above definition (see also figure 8), for $K \in \mathcal{M}_{\nu_m}$, ν_m is replaced by $\nu_f(\nu_m)$ in dof_K (and K is added to $\text{dof}_{\nu_f(\nu_m)}$). The mass exchange between matrix and DFN is accounted for by the non linear fluxes

$$F_{K\nu_f}^{\alpha}(u_{\mathcal{D}}^1, u_{\mathcal{D}}^2) = k^{\alpha}(rt_K, S^{\alpha}(rt_K, p_K)) \cdot f_{K\nu_m}^{\alpha}(u_{\mathcal{D}}^{\alpha})^{+} + k^{\alpha}(rt_K, S^{\alpha}(rt_K, p_{\nu_f})) \cdot f_{K\nu_m}^{\alpha}(u_{\mathcal{D}}^{\alpha})^{-}, \quad (13)$$

with $\nu_f = \nu_f(\nu_m)$ and $K \in \mathcal{M}_{\nu_m}$. Note that the definition (13) uses the linear fluxes $f_{K\nu_m}^{\alpha}$ to construct the non linear flux $F_{K\nu_f}^{\alpha}$. This is the key difference between this model and the continuous pressure model, which means that pressure discontinuities are accounted for in the matrix-fracture

mass exchange fluxes. For the mf -linearized model, the interfacial control volumes are set to zero, i.e. $\omega_{\nu_m} = \emptyset$ for $\nu_m \in \text{dof}_{\mathcal{D}_m}^\Gamma$. Equation (12) becomes (for all $n \in \{1, \dots, N\}$)

$$\sum_{K \in \mathcal{M}_{\nu_m}} f_{K\nu_m}^\alpha(u_{\mathcal{D}}^{\alpha,n}) = f_{\nu_m\nu_f}^\alpha(u_{\mathcal{D}}^{\alpha,n}) \quad \text{for all } \nu_m \in \text{dof}_{\mathcal{D}_m}^\Gamma, \quad (14)$$

again with $\nu_f = \nu_f(\nu_m)$. We see that the non linear equations have been replaced by linear equations for the interfacial unknowns, which constitutes the main advantage of this model compared with the non-linearized discontinuous hybrid-dimensional model. This is equivalent to the procedure of eliminating interfacial unknowns by harmonic averaging of the half transmissibilities for cell centered schemes, as described in [24], for example. This model will be referred to as the discontinuous hybrid-dimensional model 2, in the following.

3.4 Finite Volume Formulation of the continuous hybrid-dimensional model

Recall that for this model, $\text{dof}_{\mathcal{D}_m}^\Gamma = \emptyset$. For $K \in \mathcal{M}$ and $\nu \in \text{dof}_K \cap \text{dof}_{\mathcal{D}_f}$, we define $F_{K\nu}$ similarly to (13), but without taking into account the interfacial pressures:

$$F_{K\nu}^\alpha(u_{\mathcal{D}}^1, u_{\mathcal{D}}^2) = k^\alpha(rt_K, S^\alpha(rt_K, p_K)) \cdot f_{K\nu}^\alpha(u_{\mathcal{D}}^\alpha)^+ + k^\alpha(rt_K, S^\alpha(rt_K, p_\nu)) \cdot f_{K\nu}^\alpha(u_{\mathcal{D}}^\alpha)^-. \quad (15)$$

Note that this model can also be obtained from the mf -linearized discontinuous hybrid-dimensional model by replacing the interfacial equations (14) by the continuity of the phase pressures

$$u_{\nu_m}^\alpha = u_{\nu_f(\nu_m)}^\alpha \quad \text{for all } \nu_m \in \text{dof}_{\mathcal{D}_m}^\Gamma.$$

This choice of the mf fluxes captures the jump of the saturation at the mf interfaces and hence accounts for a matrix acting as a barrier for the non wetting phase. On the other hand, it does not provide a good approximation of the capillary pressure inside the fracture when the fracture is filled with the non wetting phase. This is the reason why the following second choice of the mf fluxes using the fracture rocktype will also be tested

$$F_{K\nu}^\alpha(u_{\mathcal{D}}^1, u_{\mathcal{D}}^2) = k^\alpha(rt_K, S^\alpha(rt_K, p_K)) \cdot f_{K\nu}^\alpha(u_{\mathcal{D}}^\alpha)^+ + k^\alpha(rt_\nu, S^\alpha(rt_\nu, p_\nu)) \cdot f_{K\nu}^\alpha(u_{\mathcal{D}}^\alpha)^-. \quad (16)$$

This second choice does not capture exactly the jump of the saturation at the mf interfaces but provides a better approximation of the capillary pressure inside the fracture when the fracture is filled with the non wetting phase. The same remark and choices apply to discontinuous hybrid-dimensional model 2.

Let us take (15) as the default choice. When it is needed to distinguish between the two models (15) and (16), let us call the first one continuous hybrid dimensional model 1 and the second one continuous hybrid dimensional model 2.

4 Tracer test case

The models in this section describe the transport of a tracer in a solvent through fractured porous media. It can be seen as a special case of the two-phase flow models presented above assuming that the phase mobilities satisfy $k^\alpha(S^\alpha) = S^\alpha$, that the capillarity vanishes and that the gravity field is set to zero. In the following, the primary unknowns are denoted by u for the pressure and c for the tracer concentration.

4.1 Analytical solution for the hybrid-dimensional model

Let us denote by (x, y) the Cartesian coordinates of \mathbf{x} and let us set $\Omega = (0, 1)^2$, $\mathbf{x}_1 = (0, \frac{1}{4})$, $\theta \in (0, \arctan(\frac{3}{4}))$, $\mathbf{x}_2 = (1, \frac{1}{4} + \tan(\theta))$. Let $\Omega_1 = \{(x, y) \in \Omega \mid y > \frac{1}{4} + x \tan(\theta)\}$, and $\Omega_2 = \Omega \setminus \bar{\Omega}_1$. We consider a single fracture defined by $\Gamma = (\mathbf{x}_1, \mathbf{x}_2) = \partial\Omega_1 \cap \partial\Omega_2$ with tangential permeability $\lambda_f > 0$, normal permeability $\lambda_{f,n}$ and width $d_f > 0$. The matrix permeability is isotropic and set to $\lambda_m = 1$.

The matrix and fracture porosities are set to $\phi_m = 1$ and $\phi_f = 1$. Let us denote the tangential and normal vectors to Γ by

$$\mathbf{t} = \begin{pmatrix} \cos(\theta) \\ \sin(\theta) \end{pmatrix}, \quad \mathbf{n} = \begin{pmatrix} -\sin(\theta) \\ \cos(\theta) \end{pmatrix}$$

Looking for a pressure solution equal to $u_{m,k}(x, y) = -x + \gamma_k$ in the matrix domains Ω_k , $k = 1, 2$, and to $u_f = 1 - x$ in the fracture leads to

$$\gamma_1 = 1 + \frac{\sin(\theta)}{2} d_f \frac{\lambda_m}{\lambda_{f,\mathbf{n}}}, \quad \gamma_2 = 1 - \frac{\sin(\theta)}{2} d_f \frac{\lambda_m}{\lambda_{f,\mathbf{n}}}.$$

for the discontinuous hybrid-dimensional models and to

$$\gamma_1 = \gamma_2 = 1$$

for the continuous hybrid-dimensional model ($u_{m,1}, u_{m,2}, u_f$) are solutions of the corresponding stationary pressure models, see [12], [10]). We deduce that the matrix velocity is equal to

$$\mathbf{q}_m = \lambda_m \begin{pmatrix} 1 \\ 0 \end{pmatrix},$$

and the tangential velocity in the fracture to

$$\mathbf{q}_f = d_f \lambda_f \cos(\theta) \mathbf{t}.$$

Note that the velocity fields are the same for the discontinuous and continuous hybrid-dimensional models. The transport model reduces, for the three hybrid-dimensional models presented in section 2, to the same following system of equations which specifies our choice of the boundary and initial conditions:

$$\left\{ \begin{array}{ll} \partial_t c_{m,k}(x, y, t) + \partial_x c_{m,k}(x, y, t) = 0 & \text{on } \Omega_k \times (0, T), \quad k = 1, 2, \\ c_{m,k}(x, y, 0) = 0 & \text{on } \Omega_k, \quad k = 1, 2, \\ c_{m,1}(0, y, t) = 1 & \text{on } (\frac{1}{4}, 1) \times (0, T), \\ c_{m,2}(0, y, t) = 1 & \text{on } (0, \frac{1}{4}) \times (0, T), \\ c_{m,2}(x, \frac{1}{4} + x \tan(\theta), t) = c_f(x, t) & \text{on } (0, 1) \times (0, T), \\ \partial_t c_f(x, t) + k \partial_x c_f(x, t) + \beta c_f(x, t) = \beta c_{m,1}(x, \frac{1}{4} + x \tan(\theta), t) & \text{on } (0, 1) \times (0, T), \\ c_f(0, t) = 1 & \text{on } (0, T), \\ c_f(x, 0) = 0 & \text{on } (0, 1), \end{array} \right. \quad (17)$$

where we have set $\lambda_m = 1$ and with $\beta = \frac{\sin(\theta)}{d_f}$ and $k = \lambda_f \cos^2(\theta)$. It is assumed that $k > 1$. This system can be integrated along the characteristics of the matrix and fracture velocity fields leading to the following analytical solution:

$$c_{m,1}(x, y, t) = \begin{cases} 0 & \text{if } t < x, \\ 1 & \text{if } t > x, \end{cases}$$

$$c_f(x, t) = \begin{cases} 0 & \text{if } t < \frac{x}{k}, \\ e^{-\frac{\beta}{k-1}(x-t)} & \text{if } \frac{x}{k} < t < x, \\ 1 & \text{if } t > x, \end{cases}$$

$$c_{m,2}(x, y, t) = \begin{cases} \text{if } y \in (0, \frac{1}{4}) \begin{cases} 0 & \text{if } t < x, \\ 1 & \text{if } t > x, \end{cases} \\ \text{if } y \in (\frac{1}{4}, \frac{1}{4} + \tan(\theta)) \begin{cases} 0 & \text{if } t < x - \frac{4y-1}{4 \tan(\theta)}, \\ c_f(\frac{4y-1}{4 \tan(\theta)}, t + \frac{4y-1}{4 \tan(\theta)} - x) & \text{if } t > x - \frac{4y-1}{4 \tan(\theta)}. \end{cases} \end{cases}$$

4.2 Analytical solution for the equi-dimensional model

Let us set $d = \frac{d_f}{\cos(\theta)}$ and denote by

$$\tilde{\Omega}_f = \{(x, y) \in \Omega \mid y - x \tan(\theta) - \frac{1}{4} \in (-\frac{d}{2}, \frac{d}{2})\},$$

the fracture domain, and by $\tilde{\Omega}_1 = \{(x, y) \in \Omega \mid y > \frac{d}{2} + \frac{1}{4} + x \tan(\theta)\}$, and $\tilde{\Omega}_2 = \{(x, y) \in \Omega \mid y < -\frac{d}{2} + \frac{1}{4} + x \tan(\theta)\}$ the matrix domains. We look for a pressure solution $u_{m,k} = -x + \bar{\gamma}_k$ in the matrix domains $\tilde{\Omega}_k$, $k = 1, 2$ and

$$u_f = 1 - \alpha_f(\mathbf{x} \cdot \mathbf{t} - \frac{\sin(\theta)}{4})\mathbf{t} + \beta_f(\mathbf{x} \cdot \mathbf{n} - \frac{\cos(\theta)}{4})\mathbf{n},$$

in the fracture domain. It results that $\alpha_f = \cos(\theta)$ and

$$\beta_f = \sin(\theta) \frac{\lambda_m}{\lambda_{f,\mathbf{n}}},$$

and

$$\begin{aligned} \bar{\gamma}_1 &= 1 - (1 - \frac{\lambda_m}{\lambda_{f,\mathbf{n}}}) \frac{d_f \sin(\theta)}{2} = \gamma_1 - \frac{d_f \sin(\theta)}{2}, \\ \bar{\gamma}_2 &= 1 + (1 - \frac{\lambda_m}{\lambda_{f,\mathbf{n}}}) \frac{d_f \sin(\theta)}{2} = \gamma_2 + \frac{d_f \sin(\theta)}{2}. \end{aligned}$$

We deduce that the pressure in the fracture domain is

$$u_f(\mathbf{x}) = 1 - x - \sin(\theta)(1 - \frac{\lambda_m}{\lambda_{f,\mathbf{n}}})d_\Gamma(\mathbf{x})$$

where $d_\Gamma(\mathbf{x}) = \mathbf{x} \cdot \mathbf{n} - \frac{\cos(\theta)}{4}$ is the distance between \mathbf{x} and Γ , and that the velocity field in the matrix is

$$\mathbf{q}_m = \lambda_m \begin{pmatrix} 1 \\ 0 \end{pmatrix},$$

and in the fracture

$$\mathbf{v}_f = -\Lambda_f \nabla u_f = \lambda_f \cos(\theta)\mathbf{t} - \lambda_m \sin(\theta)\mathbf{n}.$$

Note that \mathbf{v}_f is exactly equal to the tangential velocity $\frac{\mathbf{q}_f}{d_f}$ of the hybrid model plus the normal velocity $\mathbf{q}_m \cdot \mathbf{n} = -\lambda_m \sin(\theta)\mathbf{n}$ of the hybrid model. In that sense, the velocity fields are the same both in the matrix and in the fracture for the equi and hybrid-dimensional models for this test case. Also remark that the mean pressure in the width of the fracture is exactly equal to $1 - x$ (except at both ends of the fracture).

Let $\mathbf{v}(\mathbf{x})$ denote the velocity field equal to \mathbf{q}_m in the matrix domains and to \mathbf{v}_f in the fracture domain. The equi-dimensional tracer c is solution of the advection equation

$$\partial_t c + \text{div}(c\mathbf{v}) = 0,$$

with initial condition $c = 0$ on Ω and input condition $c = 1$ on the left boundary $x = 0$. It can be easily computed analytically using the method of characteristics.

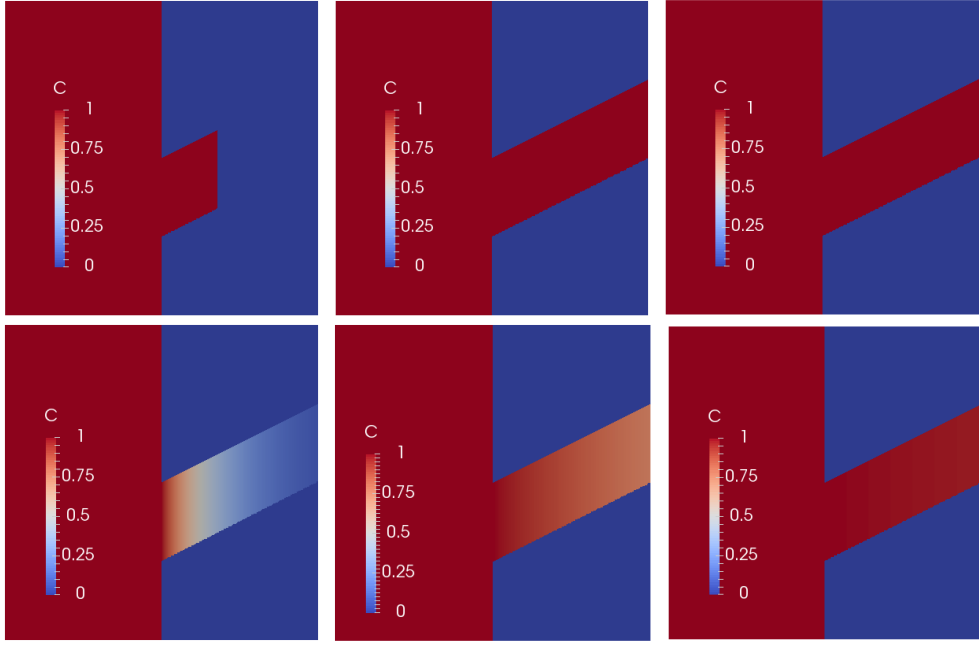


Figure 10: Comparisons of the equi-dimensional (above) and hybrid-dimensional (below) tracer analytical solutions at time $t = 0.5$ for $d_f = 0.001$, $\lambda_m = 1$, and λ_f taking the values from left to right 100, 1000 and 10000.

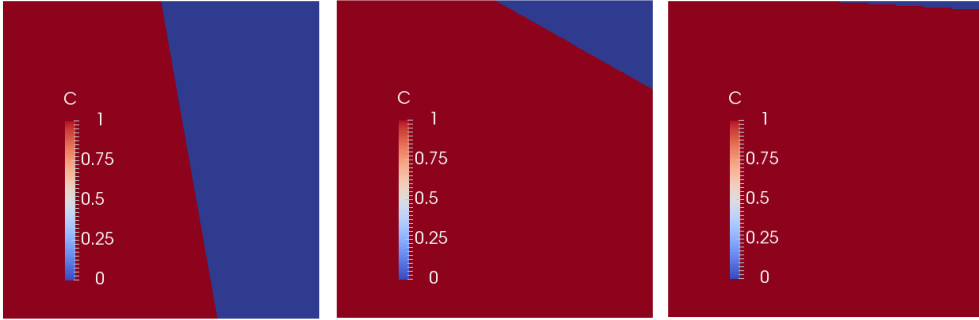


Figure 11: Tracer analytical solution in the fracture for the equi-dimensional model at time $t = 0.5$ for $d_f = 0.001$, $\lambda_m = 1$, and λ_f taking the values from left to right 100, 1000 and 10000.

4.3 Comparisons between the equi and hybrid tracer solutions

It is clear from Figures (10) and (12) that the hybrid-dimensional tracer model is accurate as long as the ratio of the fracture and matrix conductivities defined by $\frac{d_f \lambda_f}{L \lambda_m}$ is large enough where $L = 1$ denotes the characteristic length of the matrix domain. In this test case, the hybrid-dimensional tracer model provides a very accurate solution for $\frac{d_f \lambda_f}{L \lambda_m} = 10$, a rather good one for $\frac{d_f \lambda_f}{L \lambda_m} = 1$ and shows rather large differences for $\frac{d_f \lambda_f}{L \lambda_m} = 0.1$.

Geometrically, the condition of a large fracture matrix conductivity ratio $\frac{d_f \lambda_f}{L \lambda_m}$ means that the velocity in the fracture \mathbf{v}_f is almost parallel to the fracture Γ . More precisely, it prescribes that the angle between \mathbf{v}_f and \mathbf{t} is small compared with the angle between \mathbf{t} and the ligne joining the bottom left point of the fracture $(0, \frac{1}{4} - \frac{d}{2})$ to the upper right point of the fracture $(1, \frac{1}{4} + \tan(\theta) + \frac{d}{2})$.

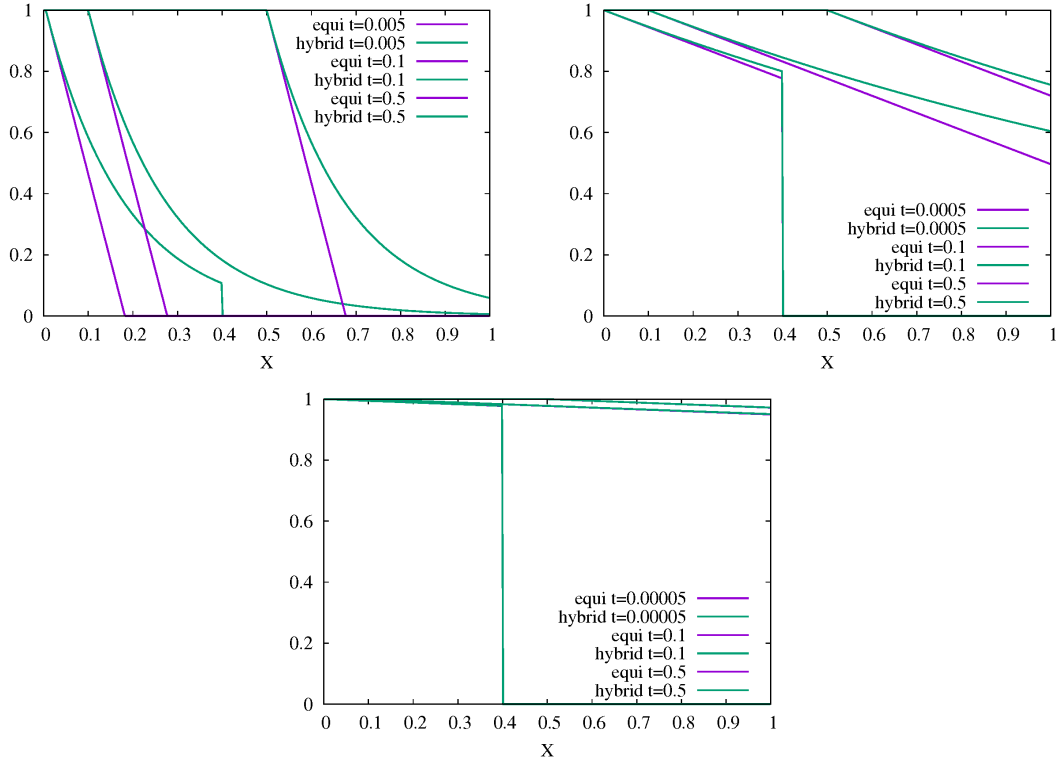


Figure 12: Comparisons of the equi and hybrid-dimensional tracer analytical solutions in the fracture at different times as a function of x . The value is averaged in the width of the fracture for the equi-dimensional model. The parameters are set to $d_f = 0.001$, $\lambda_m = 1$, and $\lambda_f = 100, 1000, 10000$ from left to right.

4.4 Comparisons between the hybrid tracer solution and the equi-dimensional tracer solution with normal diffusion in the fracture

In this test case, a normal diffusion term is added for the equi-dimensional tracer model in the fracture only. The objective is to investigate the amount of normal diffusion needed in the equi-dimensional tracer model to obtain a solution close to the hybrid-dimensional tracer model without diffusion. Since in that case the analytical solution is not known, the solution of the equi-dimensional model is computed numerically using the VAG discretization and an implicit Euler time integration. We consider the above test case with $d_f = 1$ and $\lambda_f = 100$ which exhibits rather large differences between the hybrid and the equi-dimensional tracer models without the additional diffusion term. Let \mathbf{n}_Γ denote the unit vector normal to the fracture. A diffusion term $-\text{div}(D_{f,n}\mathbf{n}_\Gamma \otimes \mathbf{n}_\Gamma \nabla c)$ is added in the equi-dimensional tracer model.

It is clear from Figures 13 and 14 and the comparison with the figures of the previous subsection that the normal diffusion in the fracture provides an equi-dimensional solution much closer to the hybrid-dimensional tracer model for the parameters $\lambda_f = 100$, $d_f = 0.001$. This is expected since the hybrid-dimensional tracer model is derived assuming that the tracer concentration is constant in the width of the fractures corresponding to a high normal diffusion $D_{f,n}$ scaled by the fracture width d_f times the normal velocity $|q_m \cdot \mathbf{n}_\Gamma|$. In our test case, this adimensionalized normal diffusion $\frac{D_{f,n}}{d_f |q_m \cdot \mathbf{n}_\Gamma|}$ takes the value $\sqrt{5}$ which suffices to recover a very good match between the equi and hybrid-dimensional models even for a rather small fracture matrix conductivity ratio $\frac{d_f \lambda_f}{L \lambda_m} = 0.1$.

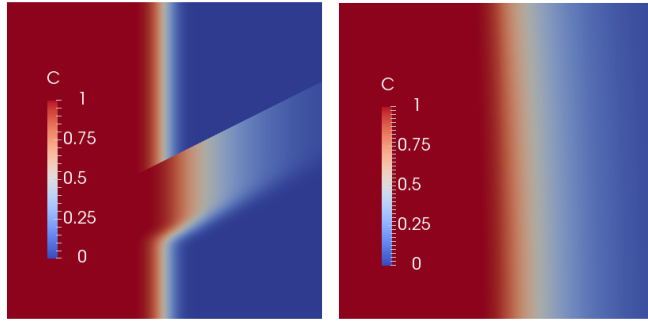


Figure 13: Tracer numerical solution at time $t = 0.5$ in the matrix (left) and in the fracture (right) for the equi-dimensional model with normal diffusion in the fracture $D_{f,n} = 0.001$ and for $d_f = 0.001$, $\lambda_m = 1$, and $\lambda_f = 100$.

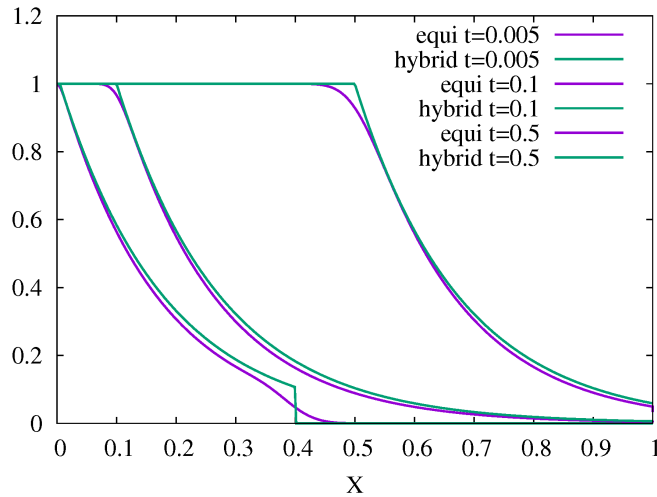


Figure 14: For $d_f = 0.001$, $\lambda_m = 1$, and $\lambda_f = 100$, comparison of the mean tracer solution in the fracture for the equi-dimensional model (numerical) with normal diffusion in the fracture $D_{f,n} = 0.001$ and the hybrid-dimensional mode (analytical).

5 Two-Phase Flow Test Cases

We present in this section a series of test cases for two-phase flow through a fractured 2 dimensional reservoir of geometry as shown in figure 15. The domain Ω is of extension $(0, 400)m \times (0, 800)m$ and the fracture width is assumed to be constantly $d_f = 4m$. This corresponds to the width of a fault, although we will keep the terminology fracture in the following. We consider isotropic permeability in the matrix and in the fractures. All tests have in common that initially, the reservoir is saturated with water (density $1000 \frac{kg}{m^3}$, viscosity $0.001 Pa.s$) and oil (density $700 \frac{kg}{m^3}$, viscosity $0.005 Pa.s$) is injected in the bottom fracture, which is managed by imposing non-homogeneous Neumann conditions at the injection location. The oil then rises by gravity, thanks to its lower density compared to water and by the overpressure induced by the imposed injection rate. Also, Dirichlet boundary conditions are imposed at the upper boundary of the domain. Elsewhere, we have homogeneous Neumann conditions. The following test cases present a variety of geological and physical configurations in regard to matrix and fracture permeabilities and capillary pressure curves.

We use the VAG discretization to obtain solutions for four different models for this two-phase flow test case. In the first model, fractures are represented as geological structures of equal dimension as the matrix and therefore, we refer to this model as the equi-dimensional model. The second and third

models are the models that we presented in the first part of this paper, referred to as discontinuous hybrid-dimensional models 1 and 2, since pressure jumps at the matrix-fracture interfaces are allowed. The fourth model is the continuous hybrid-dimensional model, presented in [9] and recalled in this paper, which assumes pressure continuity across the fractures.

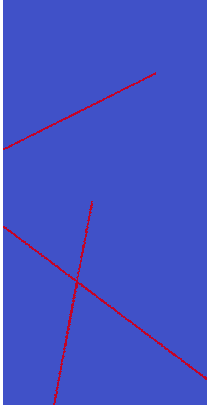


Figure 15: Geometry of the reservoir under consideration. DFN in red and matrix domain in blue. $\Omega = (0, 400)\text{m} \times (0, 800)\text{m}$ and $d_f = 4\text{m}$.

The tests are driven on triangular meshes, extended to 3D prismatic meshes by adding a second layer of nodes as a translation of the original nodes in normal direction to the plane of the original 2D domain. Hence, we double the number of nodal unknowns, while keeping the number of cell and face unknowns constant (cf. table 1). In order to account for the stratification of saturation in normal direction inside the fractures, which can play a major role in the flow process (see below), we need at least two layers of cells in the fractures for the equi-dimensional model, to obtain valid reference solutions. Obviously, the larger number of cells for the equi-dimensional mesh is due to the need of tiny cells inside the DFN. In this regard, it is worth to mention that, with the hybrid-dimensional models, the size of fracture faces is not restricted by the fracture width, while with the equi-dimensional model, the fracture width imposes an upper bound for the size of faces between the matrix and the fracture, due to mesh regularity. However, all meshes are at fracture scale, here. The mesh for the hybrid-dimensional models is the same, but the number of degrees of freedom differs. The supplementary degrees of freedom for the discontinuous models are located at

the matrix-fracture intersections and capture the pressure discontinuities, as described in the previous section.

The discrete problem is solved implicitly, where the non-linear system of equations occurring at each time step is solved via the Newton algorithm with relaxation. The stopping criterion is $crit_{Newton}^{rel}$ on the (L^1) relative residual. The resolution of the linear systems is performed by the GMRes solver (with stopping criterion $crit_{GMRes}^{rel}$ on the relative residual), preconditioned by CPR-AMG. The time loop uses adaptive time stepping, i.e. the objective for the (max per d.o.f.) change in saturation per time step, ΔS_{obj} , is given and from this the time step is deduced under the condition that it does neither exceed a given maximal time step Δt_{max} nor 1.2 times the time step of the previous iteration. Also, if at a given time iteration the Newton algorithm does not converge after 35 iterations, then the actual time step is divided by 2 and the time iteration is repeated. The number of time step failures at the end of a simulation is indicated by N_{Chop} .

Model	Nb Cells	Nb dof	Nb dof el.
equi dim.	22477	45315	22838
disc. hybrid	16889	35355	18466
cont. hybrid	16889	34291	17402

Table 1: **Nb Cells** is the number of cells of the mesh; **Nb dof** is the number of d.o.f. (with two physical primary unknowns per d.o.f.); **Nb dof el.** is the number of d.o.f. after elimination of cell unknowns without fill-in.

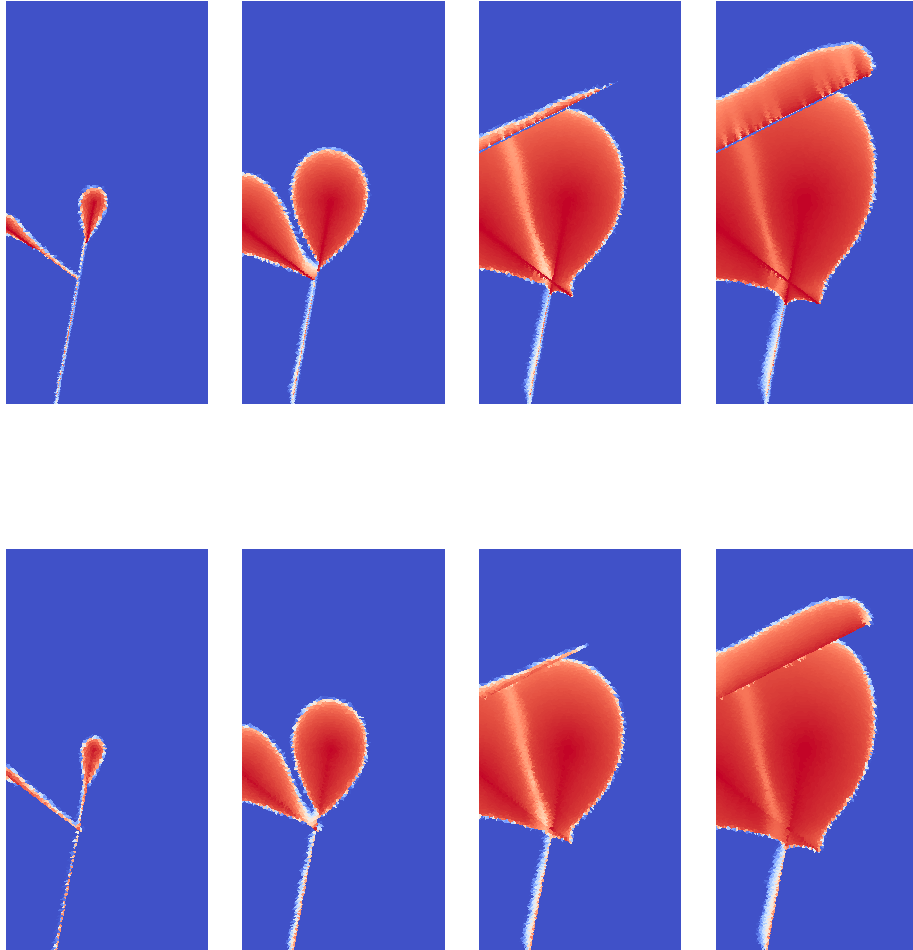
The numerical parameters are chosen as follows:

Model	$crit_{Newton}^{rel}$	$crit_{GMRes}^{rel}$	ΔS_{obj}	Δt_{max}
equi dim.	$1.E-5$	$1.E-6$	0.5	$10d$
disc. hybrid 1	$1.E-6$	$1.E-6$	0.5	$10d$
disc. 2 / cont. hybrid	$1.E-6$	$1.E-6$	0.5	$60d$

Table 2: Numerical parameters.

5.1 Comparisons between the equi and hybrid-dimensional solutions for gravity dominated flow with zero capillary pressure

In this test case, we neglect capillary effects by setting the capillary pressure to zero. To solve this problem, we use the matrix and fracture pressure and saturation (for, say, the non-wetting phase) as primary unknowns. The following geological configuration is considered. In the matrix domain, permeability is isotropic of 0.1 Darcy and porosity is 0.2. In the DFN, permeability is isotropic of 100.0 Darcy and porosity is 0.4.



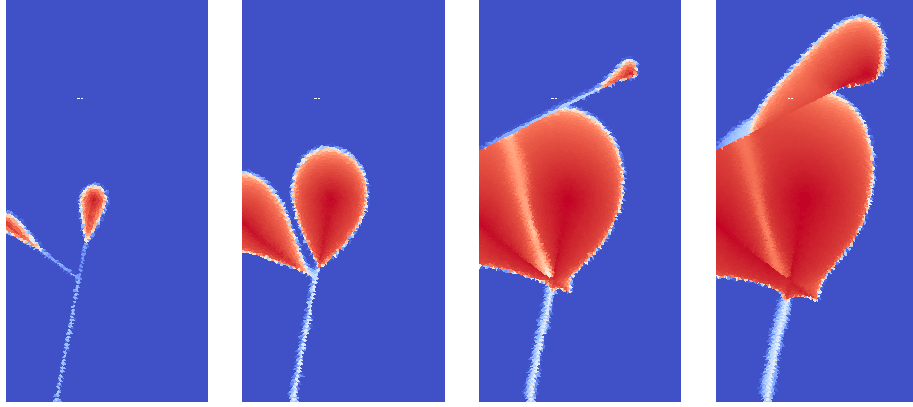


Figure 16: Comparison of the equi-dimensional (first line), discontinuous hybrid-dimensional 1 (mid line) and discontinuous 2 / continuous hybrid-dimensional (last line) numerical solutions for oil saturation at times $t = 360, 1800, 3600, 5400$ days (from left to right). Zero matrix and fracture capillary pressures and mf permeability ratio $\lambda_f/\lambda_m = 1000$.

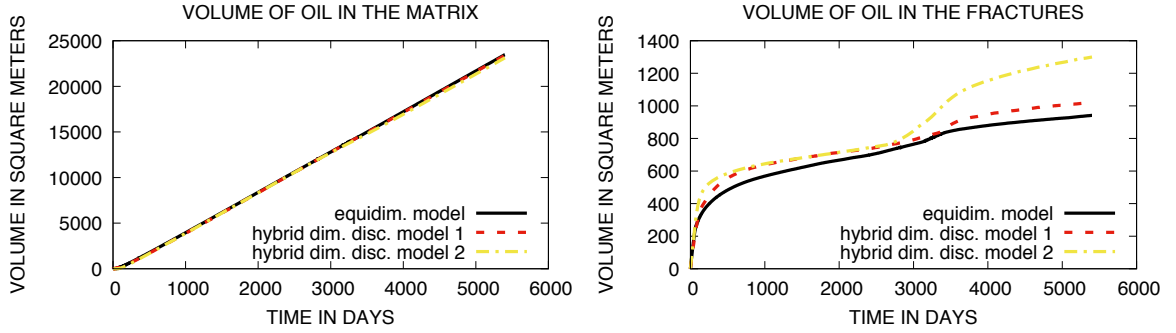


Figure 17: Comparison of the equi-dimensional and hybrid-dimensional matrix and fracture volumes occupied by oil as a function of time. Zero matrix and fracture capillary pressures and mf permeability ratio $\lambda_f/\lambda_m = 1000$.

Model	$\mathbf{N}_{\Delta t}$	\mathbf{N}_{Newton}	\mathbf{N}_{Chop}
equi dim.	1270	8927	71
disc. hybrid 1	907	5023	48
disc. hybrid 2	182	1593	0
cont. hybrid	149	1356	0

Table 3: $\mathbf{N}_{\Delta t}$ is the number of successful time steps; \mathbf{N}_{Newton} is the total number of Newton iterations (for successful time steps); \mathbf{N}_{Chop} is the number of time step chops. Zero matrix and fracture capillary pressures and mf permeability ratio $\lambda_f/\lambda_m = 1000$.

This test case shows impressively, how the incorporation of non linear normal fluxes at the mf intersections of the discontinuous hybrid-dimensional model 1 allows to get much closer to the equi-dimensional reference solution than the discontinuous 2 and continuous hybrid-dimensional models. Only one solution is presented for the discontinuous 2 and continuous hybrid-dimensional, since both models produce almost indistinguishable results. The supplementary unknowns at the mf interfaces

enable us to capture the segregation of saturation inside the DFN (due to gravity, here). In this view, the supplementary d.o.f. appear as a mesh refinement at the mf interfaces, that allows to reproduce the transport in normal direction to the DFN, which is not the case for the discontinuous 2 and continuous hybrid-dimensional models, since there, saturations at the interfaces are not calculated, but fracture saturations are used for the upwinding in the non linear mf fluxes. In the gravity dominated test case shown in figure 16, this becomes particularly important, when gravitational acceleration is in a steep angle to the fracture network, which can be observed at the upper fracture. The drawback of this feature is that we have to deal with small accumulation volumes at the mf intersections, which is reflected in terms of robustness, but the hybrid-dimensional model is still much more robust than the full equi-dimensional model. The absence of capillarity, of course, emphasizes this difference between the hybrid-dimensional models, since at the mf interfaces, the matrix does not behave as a capillary barrier (saturation does not jump) and nothing holds back the oil from leaving the DFN. Also no capillary diffusion inside the fracture prevents the gravity segregation effect in the normal direction of the fracture.

5.2 Comparisons between the equi and hybrid-dimensional solutions for gravity dominated flow with discontinuous capillary pressure

The tests presented here account for capillarity. Inside the matrix domain the capillary pressure function is given by Corey's law $p_m = -a_m \log(1 - S_m^1)$. Inside the fracture network, we suppose $p_f = -a_f \log(1 - S_f^1)$. The hybrid-dimensional models presented in the previous part of this paper are built to account for saturation jumps at the matrix-fracture interfaces (cf. figure 4). To treat the degenerated case of $a_f = 0$, we adopt a novel variable switch technique presented in [10]. This consists of introducing generalized variables as primary unknowns, that are used to parametrize the saturation and capillary pressure curves in order to avoid singularities at the heterogeneities. As a counterpart, for the discontinuous hybrid-dimensional model 1, the derivatives w.r.t. the generalized variables of the saturation at the matrix side of the mf interfaces is zero, for certain values of these generalized variables. To ensure a non singular Jacobian, we replace the accumulation terms occurring in the equations (12) for $\nu_m \in \text{dof}_{\mathcal{D}_m}^\Gamma$ by

$$\frac{1}{2} \sum_{K \in \mathcal{M}_{\nu_m}} |\omega_{K, \nu_m}| \phi_K \left(\frac{S^\alpha(rt_K, p_{\nu_m}^n) - S^\alpha(rt_K, p_{\nu_m}^{n-1})}{\Delta t^n} + \frac{S^\alpha(rt_{\nu_f}, p_{\nu_m}^n) - S^\alpha(rt_{\nu_f}, p_{\nu_m}^{n-1})}{\Delta t^n} \right)$$

with $\nu_f = \nu_f(\nu_m)$. This formula is volume conservative. It is important to note that the interfacial volumes $\omega_K^{\nu_m}$, $\nu_m \in \text{dof}_{\mathcal{D}_m}^\Gamma$, have to be chosen small in comparison with the fracture volumes. Otherwise, the discretization would artificially widen the drain, as discussed in [10] for the continuous hybrid-dimensional model.

5.2.1 drain-matrix permeability ratio of 1000

The geological setting is as follows. In the matrix domain, permeability is isotropic of 0.1 Darcy and porosity is 0.2. In the DFN, permeability is isotropic of 100.0 Darcy and porosity is 0.4. The Corey parameters are $a_m = 10^5$ and $a_f = 0$.

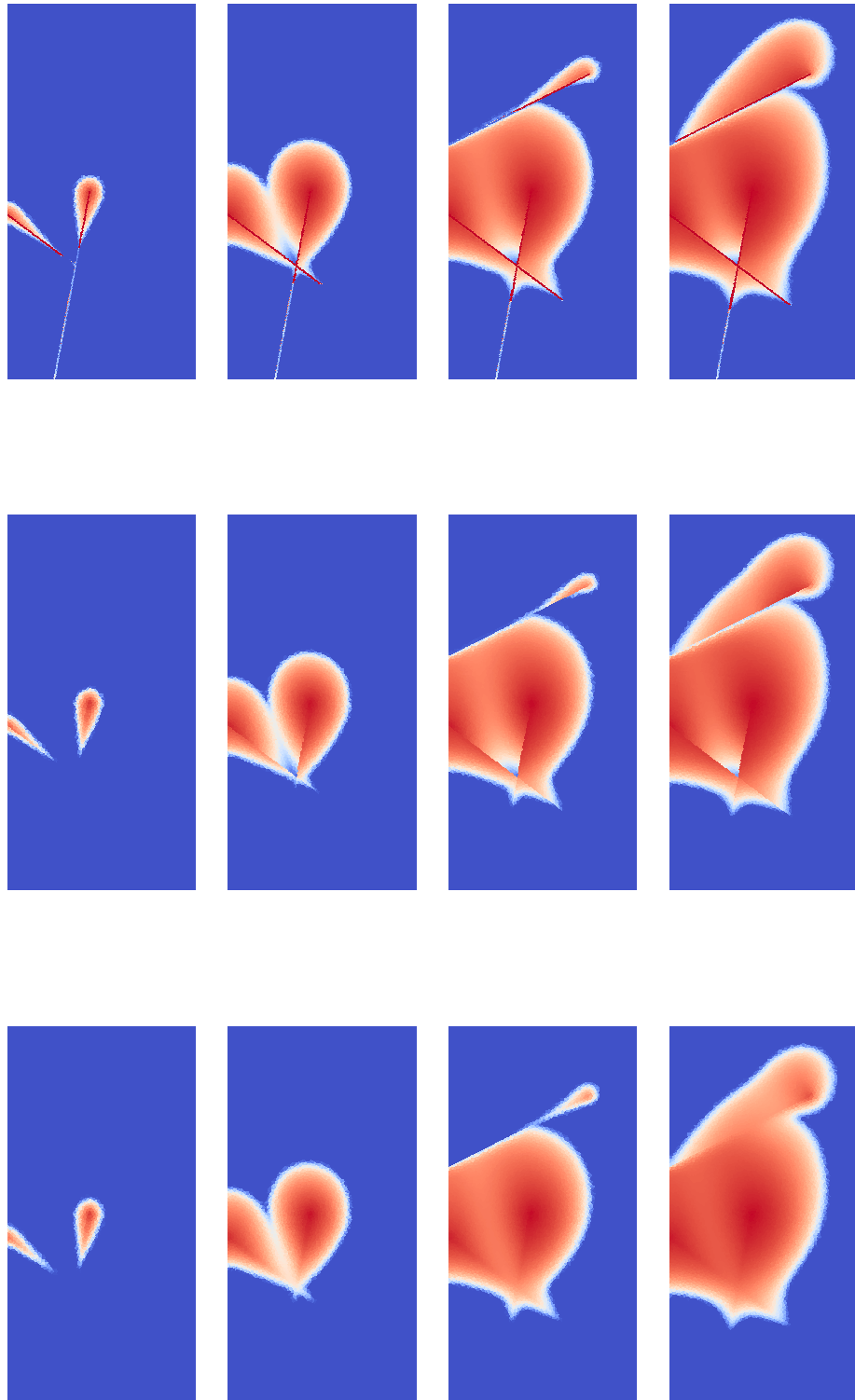


Figure 18: Comparison of the equi-dimensional (first line), discontinuous hybrid-dimensional 1 (mid line) and discontinuous 2 / continuous hybrid-dimensional (last line) numerical solutions for oil saturation at times $t = 360, 1800, 3600, 5400$ days (from left to right). Corey parameters are $a_m = 10^5$, $a_f = 0$ and mf permeability ratio $\lambda_f/\lambda_m = 1000$. The mf fluxes (15) are used for the discontinuous 2 / continuous hybrid-dimensional model.

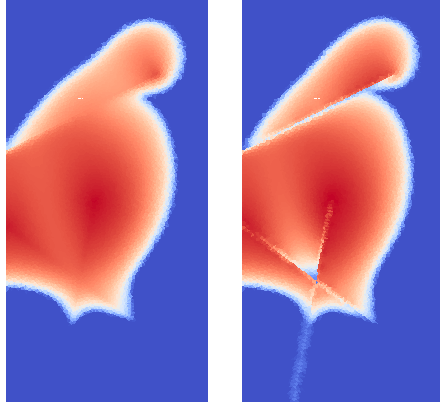


Figure 19: Comparison of the oil saturations at time 5400 days obtained with the continuous hybrid-dimensional using the mf fluxes (15) (left) and the mf fluxes (16) (right). Corey parameters are $a_m = 10^5$, $a_f = 0$ and mf permeability ratio $\lambda_f/\lambda_m = 1000$.

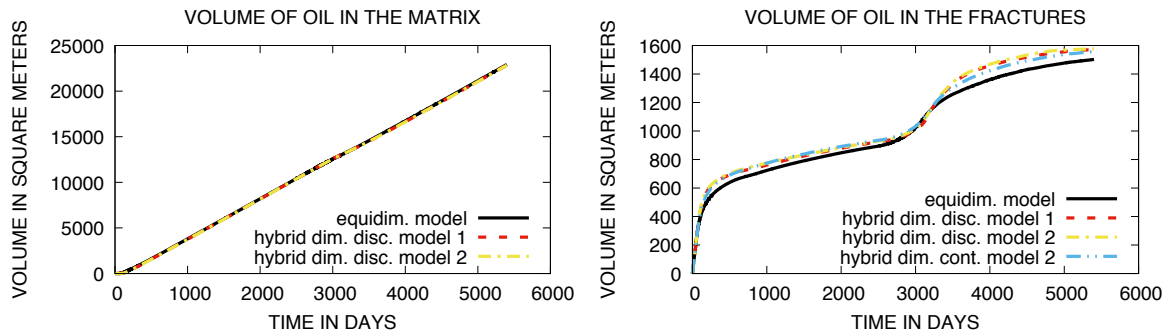


Figure 20: Comparison of the equi-dimensional and hybrid-dimensional matrix and fracture volumes occupied by oil as a function of time. Corey parameters are $a_m = 10^5$, $a_f = 0$ and mf permeability ratio $\lambda_f/\lambda_m = 1000$.

Model	$\mathbf{N}_{\Delta t}$	\mathbf{N}_{Newton}	\mathbf{N}_{Chop}
equi dim.	3054	18993	406
disc. hybrid 1	1530	7839	20
disc. hybrid 2	271	2010	1
cont. hybrid 1	149	1477	0
cont. hybrid 2	149	1418	0

Table 4: $\mathbf{N}_{\Delta t}$ is the number of successful time steps; \mathbf{N}_{Newton} is the total number of Newton iterations (for successful time steps); \mathbf{N}_{Chop} is the number of time step chops. Corey parameters are $a_m = 10^5$, $a_f = 0$ and mf permeability ratio $\lambda_f/\lambda_m = 1000$.

5.2.2 drain-matrix permeability ratio of 100

The geological setting is as follows. In the matrix domain, permeability is isotropic of 0.1 Darcy and porosity is 0.2. In the DFN, permeability is isotropic of 10.0 Darcy and porosity is 0.4.

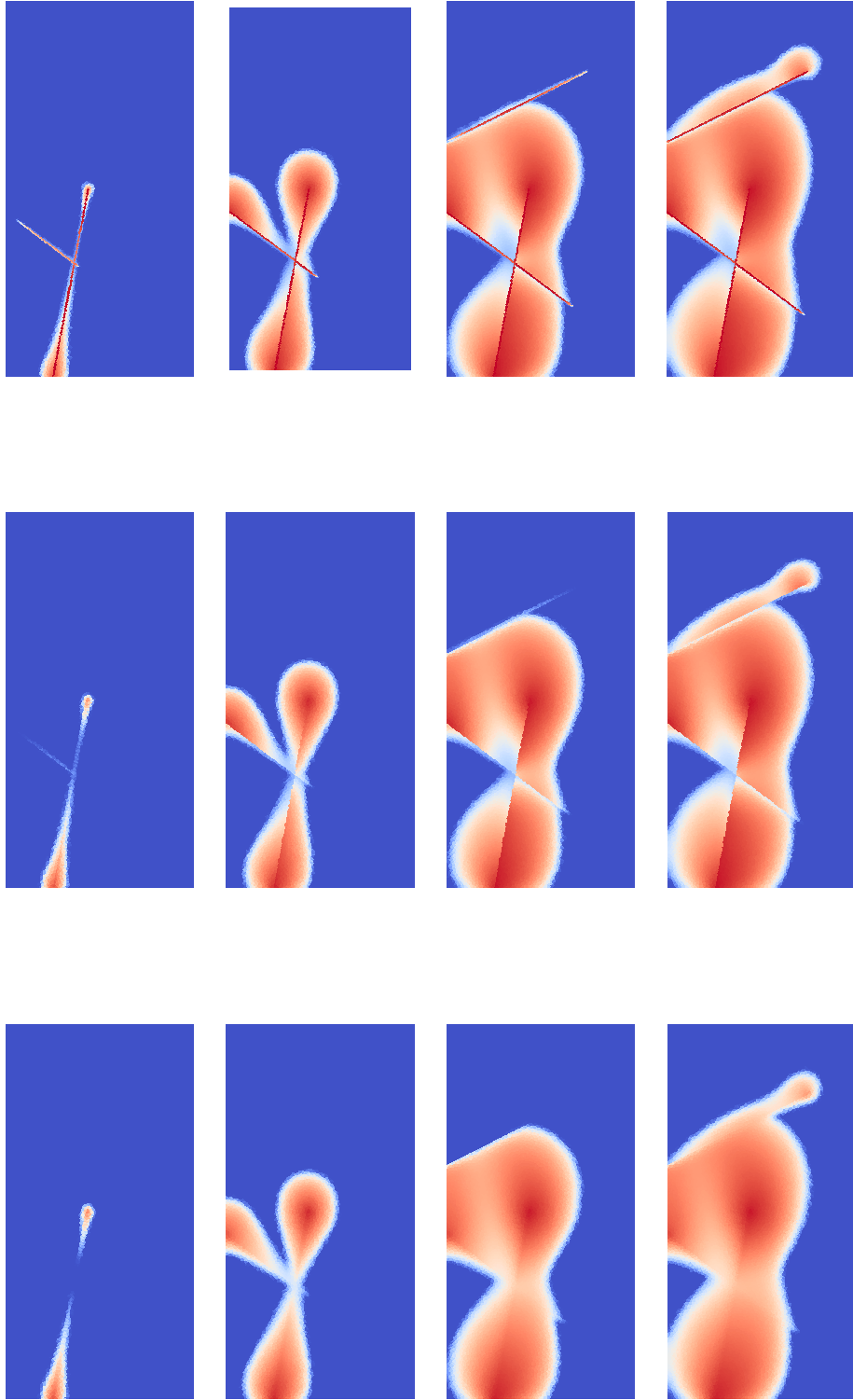


Figure 21: Comparison of the equi-dimensional (first line), discontinuous hybrid-dimensional 1 (mid line) and discontinuous 2 / continuous hybrid-dimensional (last line) numerical solutions for oil saturation at times $t = 360, 1800, 4320, 5400$ days (from left to right). Corey parameters are $a_m = 10^5$, $a_f = 10^4$ and mf permeability ratio $\lambda_f/\lambda_m = 100$. The mf fluxes (15) are used for the discontinuous 2 / continuous hybrid-dimensional model.

zero capillary pressure in the DFN: The Corey parameters are $a_m = 10^5$ and $a_f = 0$.

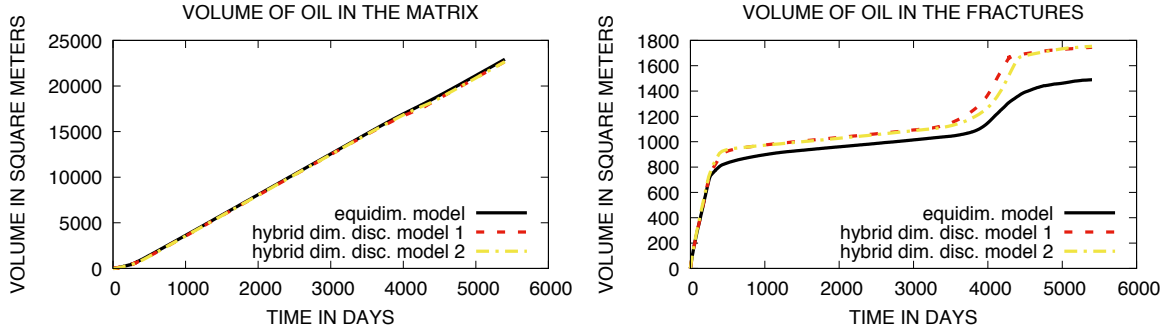


Figure 22: Comparison of the equi-dimensional and hybrid-dimensional matrix and fracture volumes occupied by oil as a function of time. Corey parameters are $a_m = 10^5$, $a_f = 0$ and mf permeability ratio $\lambda_f/\lambda_m = 100$.

Model	$\mathbf{N}_{\Delta t}$	\mathbf{N}_{Newton}	\mathbf{N}_{Chop}
equi dim.	933	6552	30
disc. hybrid 1	1182	5619	19
disc. hybrid 2	185	1196	0
cont. hybrid	149	1082	0

Table 5: $\mathbf{N}_{\Delta t}$ is the number of successful time steps; \mathbf{N}_{Newton} is the total number of Newton iterations (for successful time steps); \mathbf{N}_{Chop} is the number of time step chops. Corey parameters are $a_m = 10^5$, $a_f = 0$ and mf permeability ratio $\lambda_f/\lambda_m = 100$.

non-zero capillary pressure in the DFN: The Corey parameters are $a_m = 10^5$ and $a_f = 10^4$.

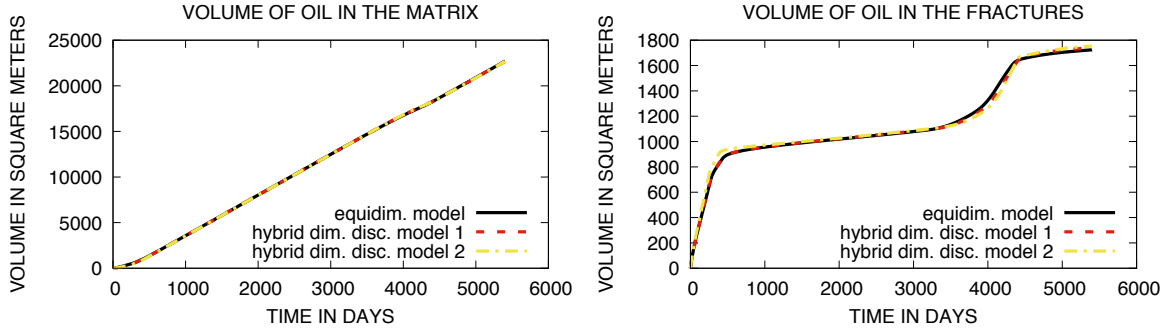


Figure 23: Comparison of the equi-dimensional and hybrid-dimensional matrix and fracture volumes occupied by oil as a function of time. Corey parameters are $a_m = 10^5$, $a_f = 10^4$ and mf permeability ratio $\lambda_f/\lambda_m = 100$.

Model	$\mathbf{N}_{\Delta t}$	\mathbf{N}_{Newton}	\mathbf{N}_{Chop}
equi dim.	610	2697	6
disc. hybrid 1	188	1243	5
disc. hybrid 2	154	801	0
cont. hybrid	192	1222	0

Table 6: $\mathbf{N}_{\Delta t}$ is the number of successful time steps; \mathbf{N}_{Newton} is the total number of Newton iterations (for successful time steps); \mathbf{N}_{Chop} is the number of time step chops. Corey parameters are $a_m = 10^5$, $a_f = 10^4$ and mf permeability ratio $\lambda_f/\lambda_m = 100$.

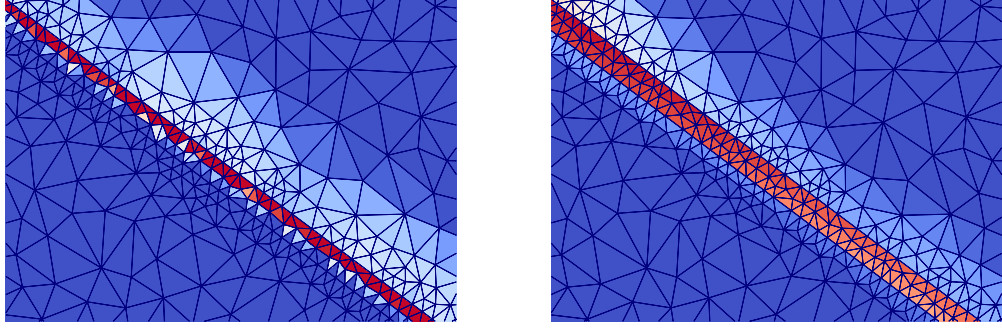


Figure 24: Zoom on bottom DFN. Comparison of the equi-dimensional oil saturation stratification in the fractures for Corey parameters $a_f = 0$ (left) and $a_f = 1.E4$ (right) at time $t = 360$ days.

We observe a degradation of the hybrid-dimensional solutions w.r.t. the equi-dimensional solution, when the mf permeability ratio decreases. This is due to the decrease of the mf conductivity ratio as already observed for the tracer test case in subsection 4.3. Figures 22 and 23 reveal that the matching of equi- and hybrid-dimensional solutions can be enhanced by adding capillarity in the DFN. More precisely, we note that the hybrid-dimensional solutions change insignificantly, but the equi-dimensional solution changes towards the hybrid-dimensional solutions. Capillarity has a diffusive effect and smoothens out the stratification in the DFN, as shown in figure 24, which agrees better with the hybrid-dimensional approach of averaging physical quantities over the fracture width. This effect is in analogy to the transport problem with normal diffusion in the fracture, as given in section 4.4. It is checked by comparing Figure 18 and the left picture of Figure 19 that the discontinuous 2 and continuous hybrid-dimensional solutions are almost indistinguishable. On the other hand, Figure 19 exhibits that the solution of both models depends strongly on the choice of the mf fluxes given either by (15) or by (16). For (15), we observe as expected that (i) oil does not penetrate in the matrix from the portion of the bottom fracture which is not yet saturated with oil, and (ii) the barrier effect of the matrix is reduced compared with the equi-dimensional or discontinuous hybrid-dimensional model 1 solutions at the mf interfaces saturated with oil. On the other hand, for (16), (i) oil penetrates in the matrix even when the fracture is not yet saturated with oil, and (ii) the barrier effect of the matrix is better reproduced. The discontinuous hybrid-dimensional model does not suffer from these difficulties since it distinguishes the unknowns at the interfaces capturing the saturation jumps and the unknowns inside the fracture providing for this test case a zero capillary pressure as expected.

5.3 Comparisons between the equi and hybrid-dimensional solutions for gravity dominated flow with discontinuous capillary pressure at the matrix-drain interfaces and an upper barrier of matrix rock type

In the matrix domain, permeability is isotropic of 0.1 Darcy and porosity is 0.2. The two lower fractures are drains of isotropic permeability 100.0 Darcy and porosity 0.4. In the upper fracture, permeability is isotropic of 0.001 Darcy and porosity is 0.2. Note that the continuous hybrid-dimensional model does not incorporate a normal permeability in the DFN. We conducted the test case also for this model and observed, as expected, the inability to reproduce the barrier behaviour of the upper fracture. The Corey parameters are $a_m = a_{barrier} = 10^5$ and $a_{drain} = 0$.

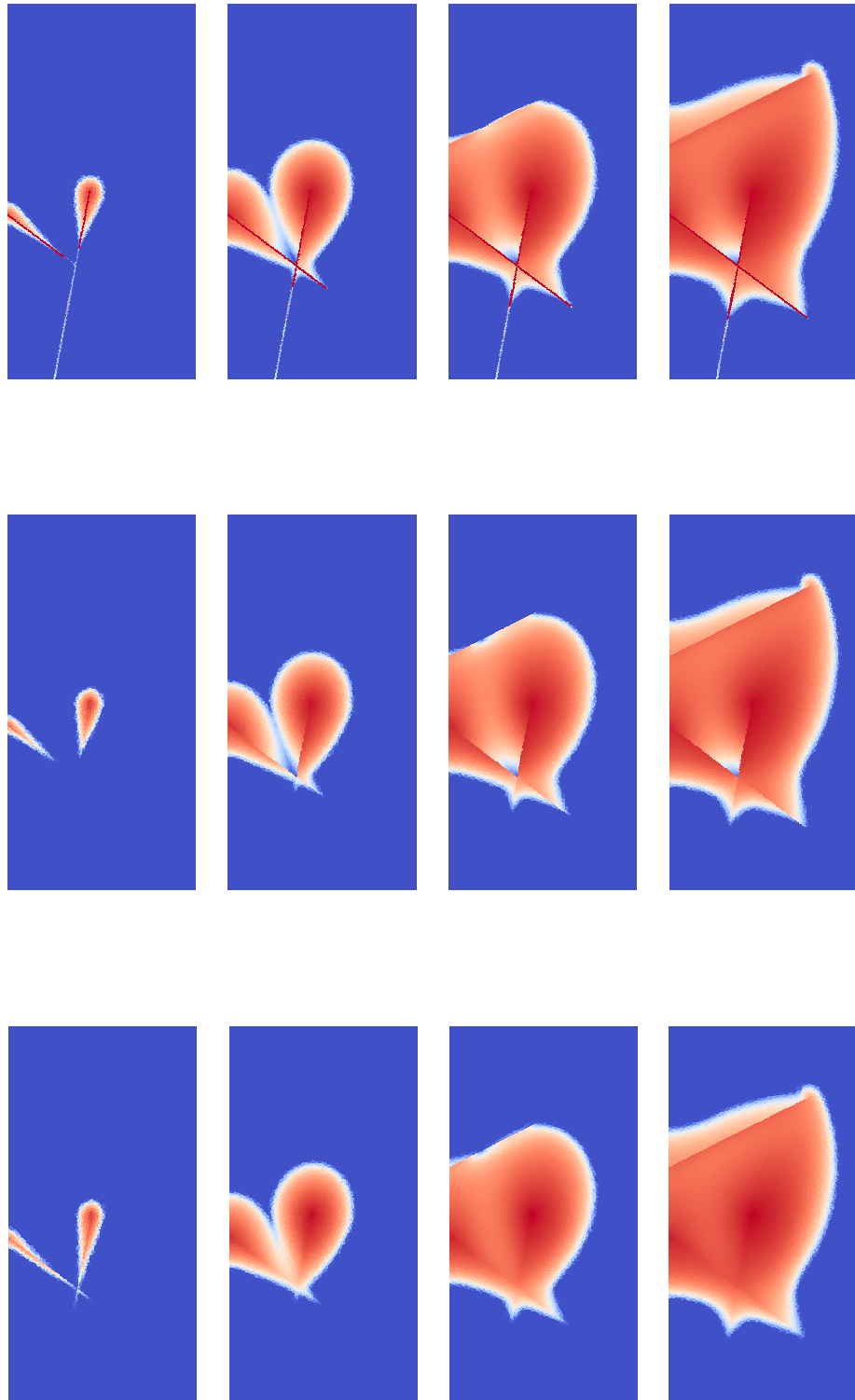


Figure 25: Comparison of the equi-dimensional (first line), discontinuous hybrid-dimensional 1 (second line) and discontinuous hybrid-dimensional 2 (last line) numerical solutions for oil saturation at times $t = 360, 1800, 3600, 5400$ days (from left to right). Corey parameters are $a_m = a_{barrier} = 10^5$, $a_{drain} = 0$ and mf permeability ratios $\lambda_{barrier}/\lambda_m = 0.01$ and $\lambda_{drain}/\lambda_m = 1000$.

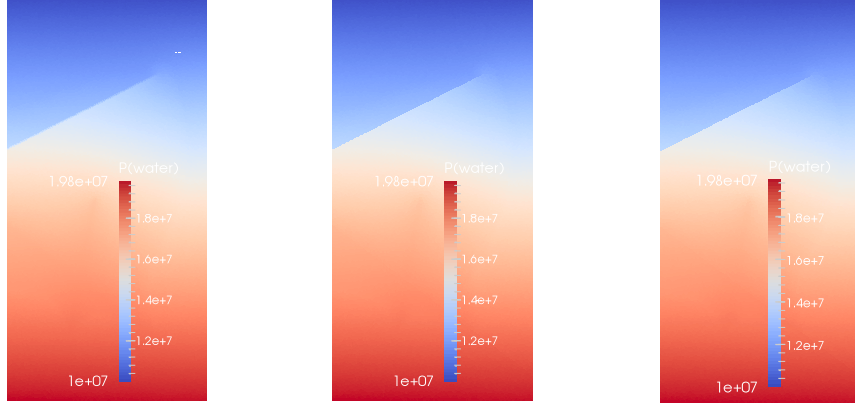


Figure 26: Comparison of the equi-dimensional, discontinuous hybrid-dimensional 1 and discontinuous hybrid-dimensional 2 numerical liquid pressure at time $t = 5400$ days (from left to right). Corey parameters are $a_m = a_{barrier} = 10^5$, $a_{drain} = 0$ and mf permeability ratios $\lambda_{barrier}/\lambda_m = 0.01$ and $\lambda_{drain}/\lambda_m = 1000$.

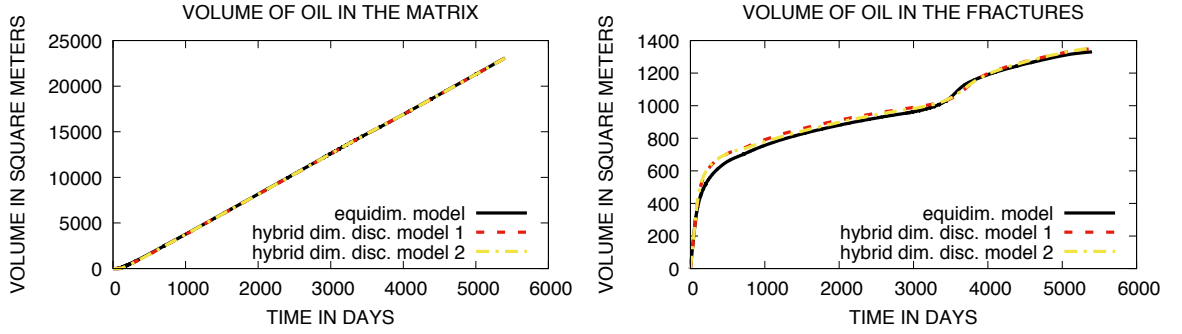


Figure 27: Comparison of the equi-dimensional and hybrid-dimensional matrix and fracture volumes occupied by oil as a function of time. Corey parameters are $a_m = a_{barrier} = 10^5$, $a_{drain} = 0$ and mf permeability ratios $\lambda_{barrier}/\lambda_m = 0.01$ and $\lambda_{drain}/\lambda_m = 1000$.

Model	$N_{\Delta t}$	N_{Newton}	N_{Chop}
equi dim.	2777	15518	376
disc. hybrid 1	1305	6444	9
disc. hybrid 2	241	1676	1

Table 7: $N_{\Delta t}$ is the number of successful time steps; N_{Newton} is the total number of Newton iterations (for successful time steps); N_{Chop} is the number of time step chops. Corey parameters are $a_m = a_{barrier} = 10^5$, $a_{drain} = 0$ and mf permeability ratios $\lambda_{barrier}/\lambda_m = 0.01$ and $\lambda_{drain}/\lambda_m = 1000$.

6 Conclusion

The discontinuous hybrid-dimensional models 1 and 2 for two-phase flow through fractured porous media with pressure discontinuities at the matrix-fracture (mf) interfaces introduced here account for network of fractures acting both as drains or barrier, general and discontinuous capillary pressures, and gravity forces. It is compared with the equi-dimensional model on various tracer and two-phase

flow test cases. For the tracer problem with a fracture dividing the matrix domain, analytical solutions for different model parameters have been derived, both, for the hybrid- and equi-dimensional models. It turned out that the hybrid-dimensional models lose in precision with decreasing conductivity ratios $\frac{d_f \lambda_f}{L \lambda_m}$, which corresponds to steepening the angle between the equi-dimensional velocity inside the fracture and the fracture tangential directions. Then, it has been shown that adding a small normal diffusion, of the order of the normal convective flux divided by the fracture width or larger, in the fracture drives the equi-dimensional solution very close to the hybrid-dimensional solution. It was expected since the averaging procedure in the derivation of the reduced models corresponds to add a diffusion in the normal direction inside the fracture network. This translates to the two-phase flow tests, as described below. The Vertex Aproximate Gradient (VAG) scheme, as introduced in [12] for the single-phase stationary hybrid-dimensional model, has been presented in a finite volume formulation for the two-phase flow models. The VAG scheme is used to compare the numerically derived solutions of four different models for a 2D flow process through a faulted reservoir. More precisely, the discontinuous hybrid-dimensional solutions (models 1 and 2 derived in this paper) have been compared to the continuous hybrid-dimensional solution (cf. [9]) w.r.t. a reference solution given by the equi-dimensional model (full model with fractures represented as heterogeneous layers), for a variety of geological and physical configurations in regard to matrix and fracture permeabilities and capillary pressure curves. Since the stratification in normal direction inside the fractures can play a major role, it is worth to mention that more than one layer of fracture cells is necessary in order to get valid reference solutions. We observed, that the discontinuous 2 and continuous hybrid-dimensional models produce solutions, which are almost indistinguishable. In terms of robustness, the test cases show that these models have a clear advantage. Yet, the discontinuous hybrid-dimensional model 1 still is much more robust than the equi-dimensional model. Moreover, for fracture matrix conductivity ratios $\frac{d_f \lambda_f}{L \lambda_m} > 10$, the equi-dimensional model is unpracticable. As for the transport problem, we observed that for high fracture matrix conductivity ratios, the equi- and hybrid-dimensional solutions match well and that for lower conductivity ratios, they differ more. On the other hand, by adding capillarity in the DFN, the hybrid-dimensional solutions fit much more to the equi-dimensional solution. In fact, the equi-dimensional solution moves towards the hybrid-dimensional solutions. In the first test case, gravitational segregation has a major influence on the global flow behaviour. This effect cannot be reproduced by the discontinuous 2 and continuous hybrid-dimensional models, with single unknowns for the saturation at the DFN and instantaneous normal transport between the interior of the fractures and the mf interfaces. This remark applies to any cell centered scheme. The supplementary information on the saturations at the mf interfaces used in the mf mass exchange fluxes of the discontinuous hybrid-dimensional model 1 enables us to capture gravitational segregation inside the DFN. Furthermore, in the examples given with capillary pressure in the matrix domain, it appears that model 1, using both interface and average capillary pressure unknowns in the fracture, restores the forces due to the capillary pressure difference between the mf interfaces and the interior of the fractures, whereas for the discontinuous 2 and continuous hybrid-dimensional models, the capillary pressure is taken constant accross the fractures, for the construction of the mf mass exchange fluxes. These features make model 1 much more precise on the transport accross the DFN compared with the discontinuous hybrid-dimensional model 2 and the continuous hybrid dimensional model which cannot both capture the saturation jump at the interface and provide a good approximation of the capillary pressure inside the fracture. Due to the assumption of pressure continuity at the mf interfaces (and the induced absence of $\lambda_{f,n}$ as a model parameter), the continuous hybrid-dimensional model is unusable, when it comes to the simulation of barriers. In the barrier test case presented here, we see that the discontinuous hybrid-dimensional models 1 and 2 perform well, both, in terms of accuracy and robustness. In any case, we observed a significant gain in precision for the discontinuous 1 hybrid-dimensional solution w.r.t. the equi-dimensional reference solution, compared to the discontinuous 2 and continuous hybrid-dimensional solutions.

Acknowledgements: The authors would like to thank Total SA for its financial support and for

allowing the publication of this work.

References

- [1] Ahmed, R., Edwards, M.G., Lamine, S., Huisman, B.A.H., Control-volume distributed multi-point flux approximation coupled with a lower-dimensional fracture model, *J. Comp. Physics*, 462-489, Vol. 284, 2015.
- [2] Ahmed, E., M., Jaffré, J., Roberts, J. E., A reduced fracture model for two-phase flow with different rock types, *Math. Comput. Simulation* (2016), <http://dx.doi.org/10.1016/j.matcom.2016.10.005>
- [3] Alboin, C., Jaffré, J., Roberts, J., Serres, C.: Modeling fractures as interfaces for flow and transport in porous media. *Fluid flow and transport in porous media* 295, 13-24 (2002).
- [4] Finite volume approximation of a diffusion-dissolution model and application to nuclear waste storage, Angelini, O., Chavant, C., Chénier, E., Eymard, R., Granet, S. *Math. Comput. Simulation* (2010), doi:10.1016/j.matcom.2010.12.016
- [5] D'Angelo, C., Scotti, A.: A mixed finite element method for Darcy flow in fractured porous media with non-matching grids. *ESAIM Mathematical Modelling and Numerical Analysis* 46,2, 465-489 (2012).
- [6] Angot, P., Boyer, F., Hubert, F. Asymptotic and numerical modelling of flows in fractured porous media, *M2AN*, 2009.
- [7] Antonietti, P.F., Formaggia, L., Scotti, A., Verani, M., Verzotti, N. Mimetic Finite Difference Approximation of flows in Fractured Porous Media, *MOX Report No 20/2015*, 2015.
- [8] Bogdanov, I., Mourzenko, V., Thovert, J.-F., Adler, P. M., Two-phase flow through fractured porous media, *Physical Review E* 68, 026703 (2003); doi: 10.1103/PhysRevE.68.026703
- [9] Brenner, K., Groza, M., Guichard, C., Masson, R. Vertex Approximate Gradient Scheme for Hybrid-Dimensional Two-Phase Darcy Flows in Fractured Porous Media. *ESAIM Mathematical Modelling and Numerical Analysis*, 49, 303-330 (2015).
- [10] Brenner, K., Groza, M., Jeannin, L., Masson, R., Pellerin, J. Immiscible two-phase Darcy flow model accounting for vanishing and discontinuous capillary pressures: application to the flow in fractured porous media, *ECMOR XV - 15th European Conference on the Mathematics of Oil Recovery* 29 August - 1 September 2016, Amsterdam, Netherlands
- [11] Brenner, K., Groza, M., Guichard, C., Lebeau, G. and Masson, R. Gradient discretization of Hybrid-Dimensional Darcy Flows in Fractured Porous Media. *Numerische Mathematik*, 1-41.
- [12] K. Brenner; J. Hennicker; R. Masson; P. Samier. Gradient discretization of hybrid-dimensional Darcy flow in fractured porous media with discontinuous pressures at matrix-fracture interfaces *IMA Journal of Numerical Analysis* 2016; doi: 10.1093/imanum/drw044
- [13] Droniou, J., Hennicker, J., Masson, R., Numerical analysis of a two-phase flow discrete fracture model, <https://arxiv.org/abs/1612.07373>. Submitted
- [14] Eymard, R., Guichard, C., Herbin, R. Small-stencil 3D schemes for diffusive flows in porous media. *ESAIM: Mathematical Modelling and Numerical Analysis*, 46, pp. 265-290, 2010.
- [15] Eymard, R., Gallouët, T., Herbin, R.: Discretization of heterogeneous and anisotropic diffusion problems on general nonconforming meshes SUSHI: a scheme using stabilisation and hybrid interfaces. *IMA J Numer Anal* (2010) 30 (4): 1009-1043.

- [16] R. Eymard, R. Herbin, C. Guichard, R. Masson, Vertex centered discretization of compositional multiphase darcy flows on general meshes. *Comp. Geosciences*, **16**, 987-1005 (2012)
- [17] Faille, I., Fumagalli, A., Jaffré, J., Robert, J. Reduced models for flow in porous media containing faults with discretization using hybrid finite volume schemes. <https://hal-ifp.archives-ouvertes.fr/hal-01162048>
- [18] Flauraud, E., Nataf, F., Faille, I., Masson, R. Domain Decomposition for an asymptotic geological fault modeling, *Comptes Rendus à l'académie des Sciences, Mécanique*, 331, pp 849-855, 2003.
- [19] Formaggia, L., Fumagalli, A., Scotti, A., Ruffo, P.: A reduced model for Darcy's problem in networks of fractures. *ESAIM Mathematical Modelling and Numerical Analysis* 48,4, pp. 1089-1116 (2014).
- [20] Fumagalli, A., Scotti, A., An efficient XFEM approximation of Darcy flows in fractured porous media, *Oil and Gas Sciences and Technologies - Revue d'IFP Energies Nouvelles* 69,4, pp. 555-564 (2014).
- [21] Mayya Groza, Modélisation et discrétisation des écoulements diphasiques en milieux poreux avec réseaux de fractures discrètes, Thèse de Doctorat de l'Université Nice Sophia Antipolis, 2016, <https://tel.archives-ouvertes.fr/tel-01466743/document>
- [22] Hajibeygi, H., Karvounis, D. and Jenny, P., A Hierarchical FractureModel for the Iterative Multiscale Finite Volume Method, *J. Comput.Phys.* 230 (24), pp. 8729-8743 (2011), <http://dx.doi.org/10.1016/j.jcp.2011.08.021>
- [23] Hoteit, H., Firoozabadi, A. Numerical modeling of two-phase flow in heterogeneous permeable media with different capillarity pressures. *Advanced Water Resources* 31:56-73, 2008.
- [24] Karimi-Fard, M., Durlofski, L.J., Aziz, K. An efficient discrete-fracture model applicable for general-purpose reservoir simulators, *SPE journal*, june 2004.
- [25] Jaffré, J., Martin, V., Roberts, J. E. Modeling fractures and barriers as interfaces for flow in porous media, *SIAM J. Sci. Comput.* 26 (5), pp. 1667-1691, 2005.
- [26] Jaffré, J., Mnejja, M., Roberts, J. E., A discrete fracture model for two-phase flow with matrix-fracture interaction, *Procedia Computer Science* 4, pp. 967-973 (2011)
- [27] Li, L. and Lee, S.H., Efficient Field-Scale Simulation of Black Oil in a Naturally Fractured Reservoir Through Discrete Fracture Networks and Homogenized Media, *SPE Res Eval & Eng* 11 (4), pp. 750-758 (2008), <http://dx.doi.org/10.2118/103901-PA>
- [28] Monteagudo, J.E.P. and Firoozabadi, A. Control-Volume Model for Simulation of Water Injection in Fractured Media: Incorporating Matrix Heterogeneity and Reservoir Wettability Effects, *SPE Journal* 12 (3), 2007, <https://doi.org/10.2118/98108-PA>
- [29] Reichenberger, V., Jakobs, H., Bastian, P., Helmig, R.: A mixed-dimensional finite volume method for multiphase flow in fractured porous media. *Adv. Water Resources* 29, 7, 1020-1036 (2006).
- [30] Sahimi, M. Flow and transport in porous media and fractured rock: from classical methods to modern approaches. John Wiley & Sons, 2011, ISBN: 978-3-527-40485-8
- [31] Sandve, T.H., Berre, I., Nordbotten, J.M. An efficient multi-point flux approximation method for Discrete Fracture-Matrix simulations, *JCP* 231 pp. 3784-3800, 2012.
- [32] Singhal, B.B.S. and Gupta, R.P. Applied Hydrogeology of Fractured Rocks, Springer Netherlands, 2010, doi: 10.1007/978-90-481-8799-7

- [33] Tunc, X., Faille, I., Gallouët, T., Cacas, M.C., Havé, P. A model for conductive faults with non matching grids, *Comp. Geosciences*, 16, pp. 277-296, 2012.